Design of a Low Reynolds Number Propulsion System for an Autonomous Underwater Vehicle

Stephen Michael Portner

Thesis submitted to the faculty of the Virginia Polytechnic Institute and State University in partial fulfillment of the requirements for the degree of

Master of Science
In
Aerospace Engineering

Wayne L. Neu, Chair
Daniel J. Stilwell
Craig A. Woolsey

August 4, 2014
Blacksburg, VA

Keywords: Autonomous Underwater Vehicle, Low Reynolds Number, Propeller, Propulsion

Design of a Low Reynolds Number Propulsion System for an Autonomous Underwater Vehicle

Stephen Michael Portner

Abstract

A methodology for the design of small autonomous underwater vehicle propulsion systems has been developed and applied to the Virginia Tech 690 AUV. The methodology is novel in that it incorporates fast design level codes capable of predicting the viscous effects of low Reynolds number flow that is experienced by small, slow turning propellers. The methodology consists of determining the minimum induced loss lift distribution for the propeller via lifting line theory, efficient airfoil sections for the propeller via a coupled viscous-inviscid flow solver and optimization, brushless DC motor identification via ideal motor theory and total system efficiency estimates. The coupled viscous-inviscid flow solver showed low Reynolds number flow effects to be of critical importance in the propeller design. The original Virginia Tech 690 AUV propulsion system was analyzed yielding an experimental efficiency of 26.5%. A new propeller was designed based on low Reynolds number airfoil section data yielding an experimental efficiency of 42.7%. Finally, an entirely new propulsion system was designed using the methodology developed herein yielding a predicted efficiency of 57-60%.

This work was supported by the U.S. Naval Oceanographic Office.

Table of Contents

List of Figures

List of Tables

Chapter 1 Introduction

The Autonomous Underwater Vehicle (AUV) group in Virginia Tech's Autonomous Systems and Controls Lab (ASCL) has designed, prototyped and tested AUVs in recent years including the Self-Mooring AUV, 690 Survey AUV (690) and is currently working on a Trawl-Resistant Self-Mooring AUV (TRAUV). Consistent across these vehicles is the requirement for an efficient, durable and cost effective propulsion system. This paper describes a design process that acknowledges previously ignored design considerations, specifically Reynolds number effects and manufacturing limitations.

1.1 Motivation

The present work was first motivated by the need to design a propulsion system specifically for the 690. The 690 is a derivative of the Self-Mooring AUV and as such shares many design features originally including the propulsion system. During 690 field trials it was discovered that the propulsion system was significantly underperforming. An initial investigation determined the source of performance drop was because the 690 has much higher drag than the Self-Mooring AUV. The solution was to design a new propeller specifically for the 690.

While the design process for the new propeller was the same as in the past, new analysis tools including PSF10 [1] (a three-dimensional vortex lattice code specifically for propellers) and limited RANS CFD were used to predict performance. It was while learning to use these tools that the importance of Reynolds number effects became apparent.

Upon recognizing the importance of Reynolds number effects for small propellers, the motivation for the work changed reflecting a desire to develop a design procedure specific to low Reynolds number propellers.

The design task is to develop a propulsion system for the 690 that is capable of driving the AUV to a cruise velocity of 2 m/s as efficiently, reliably and cost effectively as possible. From this task follow several others, they include: propeller design, motor selection, battery voltage selection and miscellaneous small tasks such as coupling and sealing choices (how to take motor power from inside the vehicle to the propeller outside the vehicle). Each of these tasks may have open questions associated with them.

Propeller design is the largest task for several reasons. First, because the propeller diameter is constrained to be smaller than the vehicle diameter it will experience low Reynolds number effects. Traditional design methodologies weren't developed for the laminar and transitional flow experienced at the range of low Reynolds numbers expected, between 20,000 and 200,000. Second, again because the propeller is expected to be small, manufacturing becomes a problem. As will be shown, at low Reynolds numbers drag and therefore torque is proportional to the thickness of the propeller blades. This implies the thinnest blade is likely the best. Unfortunately, blade thickness is restricted by structural issues and its manufacturability. The low Reynolds number effects and manufacturing thickness limitations combine to impose strong limitations on the foil section shapes that should be used along the propeller's span. The limited literature that does exist on low Reynolds number airfoils often

proposes thickness distributions that simply can't be manufactured at reasonable cost at such small scale.

Motor selection appears to be a task well understood and straight forward if one uses ideal motor theory. Knowing the load and speed requirements for a motor makes determining the best design based on ideal motor theory very simple. Further, this motor design will then set the propulsive battery voltage. A few issues do arise in practice. One is that ideally the vehicle would operate with the motor controller at 100% duty cycle at all times. This is unlikely, however, because it is desirable to be a capable of turning the propeller at rates higher than the cruise RPM for conditions such as diving. Ideal motor theory tells us nothing about the loss of efficiency due to using a motor controller at partial duty cycle.

1.2 Previous Work

There is a vast library of literature available regarding the design of propulsion systems for both marine and air vehicles. Carlton [2] provides a good overview on marine propulsion as a whole. Unfortunately, much of the work in propeller analysis and design makes the assumption of high Reynolds number flow. While almost always a good assumption it appears to leave the field of low Reynolds number propellers undeveloped.

In recent years the topic of low Reynolds number propulsion design has appeared, with applications typically being to unmanned air vehicles (UAVs) or micro air vehicles (MAVs). Kunz [3] explored rotor design for MAVs with Reynolds numbers below 10,000 both computationally and experimentally. Deters and Selig [4] have done experimental testing of micro-propellers in additional to Selig's extensive other work with low Reynolds number airfoils which includes several volumes of low speed airfoil data [5]. Merchant [6] provides another set of low Reynolds number propeller data. Grasmeyer and Keennon [7] touch on and Turner [8] attempted the design of a MAV propulsion system with knowledge of low Reynolds number effects.

Previous work has also been performed at Virginia Tech, typically for specific vehicle designs. This includes, work on counter-rotating propeller design by Jacobson [9], and propulsion design using commercial-off-the-shelf (COTS) components by Schultz [10] and custom components by Duelley [11]. Schultz and Duelley both made use of the MATLAB program OpenProp [12] for minimum induced loss propeller design. The present work is a continuation of that by Duelley, which itself is a continuation of work by Schultz.

1.3 Thesis Organization

Chapter 2 covers most of the theory including propeller fluid dynamics, low Reynolds number flow effects and motor modeling.

Chapter 3 focuses on the proposed propulsion system design methodology.

Chapter 4 presents analysis of the original 690 propulsion system using the newly developed tools, a new propeller design using low Reynolds number wind tunnel data and an entirely new propulsion system design with new battery voltages, motors and propellers.

Chapter 5 contains a summary of the work performed and suggestions for future work.

The appendices include the works cited page, several derivations and a short list of software written for this thesis.

Chapter 2 Theory and Simulation Techniques

Design and analysis of an AUV propulsion system requires models of the propeller and motor. Typically propeller modeling requires both fluid dynamics and structural mechanics components. Due to the low loads experienced the structural problem is almost entirely ignored in this case. Motor modeling can be very complicated, but for design level tasks does not need to be.

This chapter first covers the fluid dynamics of propellers and then a simple motor model.

2.1 Fluid Dynamics

The methods of analyzing propeller hydrodynamic performance can largely be categorized by their level of complexity. The lowest level of analysis, propeller momentum theory, assumes potential flow and largely ignores the geometry of the propeller. At the next level are potential flow codes that model geometry but don't model any viscous effects. Beyond the potential flow codes are coupled viscous-inviscid flow solvers that combine potential flow codes with boundary layer solvers. The highest accuracy analysis tools are computational fluid dynamics codes that solve one version or another of the Navier-Stokes equations.

Blade element theory is a strategy for propeller modeling which assumes the propeller can be broken into strips each of which are treated independently as two-dimensional foil sections and then integrated together to determine propeller performance. Blade element theory makes no assumptions on how the strip or sectional lift and drag coefficients are determined. Therefore, while blade element theory is not complex on its own, the means of determining sectional lift and drag can be as simple as thin airfoil theory or as complex as computational fluid dynamics or wind tunnel testing.

All of the given categories of propeller modeling beyond momentum theory are used for analysis but for early stage design the potential flow codes without viscous effects are usually used. Often viscous effects will be included via sectional properties of the propeller blades in a stripwise sense. The validity of 2D airfoil data depends on blade aspect ratio with low aspect ratio blades resulting in accuracy issues due to 3D flow effects. Experimental airfoil data at the Reynolds number range of interest is limited so simulation tools for low Reynolds number airfoils are required.

Fluid dynamics tools will be presented in two groups, those that don't simulate viscosity, inviscid methods, and those that do, viscous methods.

2.1.1 Inviscid Methods

Inviscid fluid dynamic methods are those which ignore the viscosity of the fluid. Such methods are often, but not always, based on the assumption of potential flow. The performance prediction methods described here are propeller momentum theory, thin airfoil theory, panel methods and lifting line theory.

2.1.1.1 Momentum Theory

Propeller momentum theory also known as momentum disk theory or Rankine momentum theory is a simple propeller model based on axial motion of water passing through the propeller disk.

Momentum theory is based on three assumptions:

1. The propeller works in an ideal fluid and, therefore, does not experience energy losses due to frictional drag.
2. The propeller can be replaced by an actuator disc momentum source.
3. The propeller can produce thrust without causing rotation in the slipstream.

The main useful result of momentum theory is that there is an inviscid maximum efficiency. This ideal efficiency is given by equation 1,

$$\eta = \frac{2}{1+\sqrt{1+C_T}}, \quad C_T = \frac{T}{\frac{\pi}{4}D^2\frac{1}{2}\rho V^2} \tag{1}$$

Here, η is the efficiency, C_T is a thrust coefficient, T is the thrust, D is the propeller disk diameter, ρ is the fluid density and V is the free stream velocity.

A derivation for the ideal efficiency is provided in 0.

2.1.1.2 Thin Airfoil Theory

Thin airfoil theory is a simple means of using the camber line to determine airfoil lift coefficient. In addition to potential flow it makes an assumption of infinitesimal thickness. The airfoil is modeled as a series of line vortices coincident with the camber line of the airfoil. The vorticity distribution along the vortex sheet is determined such that the camber line is a streamline. Since the flow is inviscid thin airfoil theory on its own does not make drag predictions.

For a parabolic camber line thin airfoil theory can be used to determine the relationship between maximum camber and lift coefficient. Appendix B shows the details, but the main results of such an exercise for an airfoil with unit length chord, maximum camber z_{max} and maximum camber location at x = 0.5 are,

$$\mathrm{C_l} = 2\pi\alpha + 4\pi z_{max}, \tag{2}$$

$$\alpha_{0\mathrm{l}} = -2z_{max}. \tag{3}$$

Here, C_l is the section lift coefficient, α is the angle of attack in radians, z_{max} is the maximum camber and α_{0l} is the no/zero-lift angle of attack.

The zero-lift angle of attack, α_{0l}, is important because it should be the same or nearly the same for an airfoil and wing of the same sectional geometry.

2.1.1.3 Panel Methods

Panel methods, also known as boundary element methods were first developed by Hess and Smith [13]. In panel methods, the propeller is typically represented by a series of quadrilateral surfaces with source and doublet distributions to maintain the no through flow boundary condition. Panel methods have the benefit of providing the pressure distribution over the surface of the blades, modeling thickness and accurately modeling the interactions between the propeller hub and blades.

As with Thin Airfoil Theory, the only drag predicted will be induced drag which does not exist in 2D flow. Panel methods can be formulated in 3D in which case the induced drag can be calculated, however, the

induced drag is dependent on modeling the wake which is not a trivial task. Low Speed Aerodynamics [14] by Katz and Plotkin is an excellent resource on panel methods with an application based approach.

2.1.1.4 Lifting Line Theory

Lifting line theory (LLT) assumes that each section of a wing acts like an isolated two-dimensional section an assumption which depends on the magnitude of spanwise flow. LLT further assumes that section lift is related to the local circulation via the Kutta-Joukowski theorem. Using these two assumptions, LLT allows analysis of wings and propeller blades (which are effectively wings) with spanwise lift variation. A partial derivation of LLT can be found in Appendix C.

One of the key results is that the wing lift and induced drag are functions of the spanwise circulation,

$$L = \int_{-s}^{s} \rho_\infty u_\infty \Gamma(y)\, dy \tag{4}$$

$$D_i = \int_{-s}^{s} \rho_\infty \mathrm{w} \Gamma(y)\, dy \tag{5}$$

Here, L is the wing lift, s is the wing half-span,ρ_∞ is the free stream fluid density, u_∞ is the free stream velocity, $\Gamma(y)$ is the circulation at station y along the span, D_i is the lift induced drag and w is the induced downwash velocity.

This indicates that the optimal wing corresponds to an optimal circulation distribution. Coney [15] provides an excellent development of LLT based circulation optimization via calculus of variations. An optimal circulation distribution does not provide a full geometry but can be used to perform a parametric design study to determine certain parameters such as diameter and propeller turn rate. Specific sectional geometry such as camber and thickness must be determined separately from the LLT optimal design.

The optimization portion of the minimum induced loss propeller design software OpenProp is based on lifting line theory.

2.1.1.5 Other Models

Lifting surface theory tries to overcome some of the limitations of lifting line theory by replacing the blade with a thin surface shaped by the blade camber line with vorticity placed in both the chordwise and spanwise directions. Thickness effects can be achieved by incorporating source distributions.

Vortex lattice methods are a subset of lifting surface theory in which the continuous distributions of vortices and sources are replaced with a finite set of straight line elements of constant strength approximating the lifting surface.

2.1.2 Viscous Methods

Viscous methods are those simulation techniques that incorporate fluid viscosity in one way or another. Investigated techniques include coupled viscous-inviscid flow solvers and CFD.

2.1.2.1 Coupled Viscous-Inviscid Solvers

Potential flow solvers can be coupled with a boundary layer solver to incorporate viscous effects. An example of such a code is XFOIL.

In the XFOIL implementation of a coupled viscous-inviscid flow solver the inviscid problem and viscous problems are solved simultaneously. The inviscid problem is solved using linearly varying strength vortex panels maintaining continuity of the vorticity distribution on the airfoil surface and constant strength source panels on the airfoil surface and in the wake. The source panels are used to simulate the viscous boundary layer thickness.

The viscous problem is solved in XFOIL using a two-equation integral formulation based on dissipation closure for both laminar and turbulent flows. Transition is predicted based on spatial amplification theory (the e^n method). A lag equation is included in the turbulent formulation to account for lags in the response of the turbulent stresses to changing flow conditions. The reason to use the two-equation formulation is the capability to accurately model thin separated regions such as laminar separation bubbles [16].

The Newton-Raphson method is used to simultaneously solve the inviscid Euler equations and the boundary layer equations. This is different from some other coupled viscous-inviscid flow solvers which iterate between solving the inviscid problem and viscous problem sequentially.

For a full description of XFOIL see [16] and [17].

2.1.2.2 Computation Fluid Dynamics

Computation fluid dynamics (CFD) has been used to good effect with propellers as well [18]. CFD is the most expensive modeling method, with model set up and calculation taking large amounts of time. The time limitations often result in CFD being used only as an analysis tool whereas the other modeling methods mentioned can be used in design.

2.1.3 Blade Element Theory

Blade element theory (BET) assumes propeller performance can be computed by an integration of 2D sectional performance. To determine the 2D section performance, section lift and drag coefficients as well as the incident velocity are required. The incident flow velocity is composed of velocity due to axial motion of the propeller, rotational motion of the propeller and velocities induced by the propeller doing work. The components of and total incident velocity and incident velocity angle are then given as,

$$u = \omega r + V_t + u_t^*, \tag{6}$$

$$v = V_a + u_a^*, \tag{7}$$

$$V = \sqrt{u^2 + v^2},$$

$$\mathrm{B}_i = \tan^{-1}\left(\frac{V_a + u_a^*}{\omega r\, V_t + u_t^*}\right). \tag{8}$$

Here, u is the incident velocity in the torque direction, ω is the rotation rate of the propeller, r is the radius at a specific radial station, V_t is the inflow velocity in the torque direction at a specific radial station and u_t^* is the induced velocity in the circumferential direction at a specific radial station. v is the incident velocity in the opposite of the thrust direction, V_a is the inflow velocity in the opposite of the thrust direction and u_a^* is the induced velocity in the opposite of the thrust direction. V is the total incident velocity. B_i is the total incident velocity angle relative to the propeller disk plane.

The elemental torque and thrust for each section can then be computed as,

$$dQ = \frac{1}{2}\rho Z c V^2 (C_l \sin(B_i) + C_d \cos(B_i)) r \, dr \,, \tag{9}$$

$$dT = \frac{1}{2}\rho Z c V^2 (C_l \cos(B_i) - C_d \sin(B_i)) \, dr. \tag{10}$$

Here, dQ is the elemental torque, dT is the elemental thrust, Z is the number of propeller blades and c is the section chord.

With the elemental thrust and torque the efficiency of the section is given by power in over power out or,

$$\eta = \frac{V \, dT}{\omega \, dQ}. \tag{11}$$

This can be further simplified by re-writing,

$$H = \frac{C_d}{C_l}, \tag{12}$$

$$\eta = \frac{\tan(B_i)}{\tan(B_i + H)}. \tag{13}$$

To calculate performance of the propeller the elemental torque and thrust need simply be integrated, typically numerically.

2.1.4 Low Reynolds Number Effects

At high Reynolds number the lift and drag coefficients of airfoils are relatively constant with changing Reynolds number. At low Reynolds number the drag coefficient increases with decreasing Reynolds number (see **Figure 1**) and stall occurs at lower angles of attack limiting the maximum lift coefficient. This is because at high Reynolds number the airfoil will have a turbulent boundary layer while at low Reynolds number the airfoil will have a laminar or transitional boundary layer.

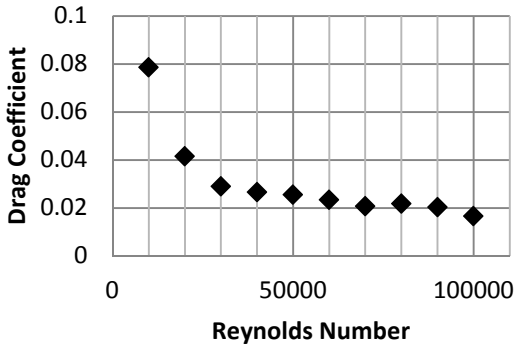

Figure 1. Drag coefficient of optimal constant thickness parabolic camber airfoils for a variety of Reynolds numbers designed using XFOIL

Laitone [19] performed a series of wind tunnel experiments looking at the performance of airfoils at low Reynolds number. Laitone found that thin constant thickness airfoils with sharp leading and trailing edges far out performed more traditional airfoil shapes at Reynolds numbers under 70,000. Laitone

suggests that the sharp leading edge is preferable because it results in a leading edge vortex that helps keep flow attached to the airfoil. This agrees with work by Kunz [3] that found while a varying thickness distribution can improve performance, usually the most important factor in performance is the maximum section thickness. Both also found that increasing Reynolds number for a design improves performance, typically by reducing drag coefficient while maintaining lift coefficient.

Both of these conclusions also agree with computational work done for this thesis. Using XFOIL, a series of optimal parabolic spline camber line airfoils were designed. The free parameters for the design were the thickness, maximum camber and position of maximum camber. As seen in **Figure 1** and **Figure 2**, the optimal lift to drag ratio monotonically increases with Reynolds number while drag coefficient decreases.

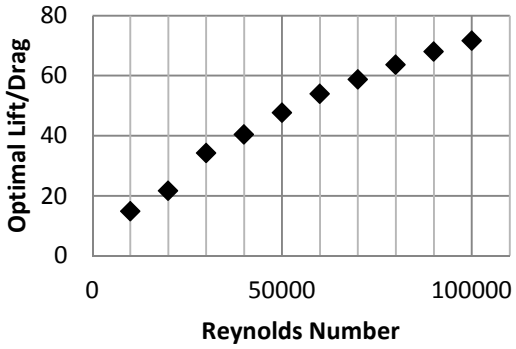

Figure 2. Lift/drag of optimal constant thickness parabolic camber airfoils for a variety of Reynolds numbers designed using XFOIL

A common feature of the boundary layer on an airfoil at low Reynolds number is the development of a laminar separation bubble, which is a region of separation early on the airfoil that re-attaches as a turbulent boundary layer. Since this is a flow feature that doesn't exist for higher Reynolds numbers, specially designed airfoils are required for low Reynolds number operation. Often, controlling the length of the separation bubble is the critical task of the low Reynolds number airfoil designer [20].

A laminar separation bubble can result in a hysteresis loop in the lift and drag vs angle of attack relationships. Figure **3** shows the hysteresis loop as found using XFOIL for a thin cambered airfoil.

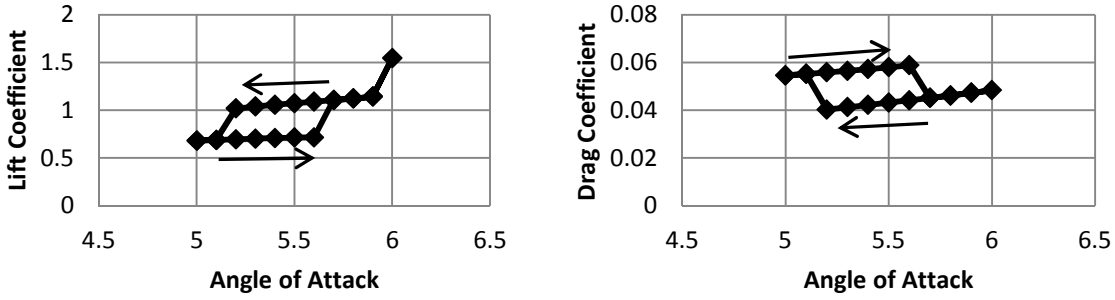

Figure 3. Lift and drag coefficient hysteresis loops with presence of laminar separation bubble

2.2 Motor Theory

Electric motors are complex physical systems, but for design level tasks simple motor models can be used. This section describes the type of motor to be utilized in the propulsion system design and a simple physical model.

2.2.1 Motor Basics

The most common type of electric motor is the magnetic motor and that is the type of interest. Magnetic motors can be categorized as either direct current (DC) or alternating current (AC) motors. The commutation scheme, that is how rotation is induced, provides another means of categorization between mechanically and electrically commutated motors. The most common type of mechanically commutated electric motor is the direct current brushed motor while a common type of electrically commutated motor is the brushless "DC" (BLDC) motor. DC is in quotes because the current in the actual motor is alternating but the supply current to the BLDC motor controller, which is considered part of the motor, is DC.

Brushed DC motors are often the simplest and cheapest available while BLDC motors are more complex and expensive due to the electric commutation. BLDC motors are more reliable with to fewer moving parts and higher efficiency since they lack brush friction. Additionally, either kind of motor can have an inner rotor or an outer rotor known as an in-runner or an out-runner, respectively. Because of their higher efficiency and reliability only BLDC motors will be considered. Additionally, due to results from Duelley [11] and the motor housing of the 690 being oil-filled for pressure compensation, an inner-rotor motor will be used.

2.2.2 Ideal Motor Equations

A derivation of the ideal motor equations is given in Appendix D. The principal results are that the following equations which are dependent on three constants specific to each motor, $K_E,\ I_{nl},\ R_s$. The motor turn rate, torque generated and efficiency are given by,

$$\omega_m = \frac{1}{K_E} E = \frac{1}{K_E}(V_m - R_s I_m), \tag{14}$$

$$Q_m = K_E(I_m - I_{nl}), \tag{15}$$

$$\eta = \frac{\omega_m T}{V_m I_m} = \frac{(V_m - R_s I_m)(I_m - I_{nl})}{V_m I_m}. \tag{16}$$

Here, ω_m is the motor turn rate, K_E, is a motor constant, E is the induced back electromotive force voltage, V_m is the voltage supplied to the motor windings, R_S is the resistance of the motor windings, and I_m is the current supplied to the motor windings. K_E is often referred to as K_Q since it relates torque to current and when inverted is often referred to as $K_v = \frac{1}{K_E}$ since it relates voltage to motor turn rate. Q_m is the motor torque and I_{nl} is the no-load current of the motor, another motor constant.

And the performance at maximum efficiency is given by,

$$I_{\eta,max} = \sqrt{\frac{V_m I_{nl}}{R_s}} \tag{17}$$

$$\eta_{max} = \left(1 - \sqrt{\frac{I_{nl}R_s}{V_m}}\right)^2, \tag{18}$$

$$\omega_{m,\eta_{max}} = \frac{1}{K_E}\left(V_m - R_s I_{\eta_{max}}\right) \tag{19}$$

$$Q_{\eta_{max}} = K_E\left(I_{\eta_{max}} - I_{nl}\right). \tag{20}$$

Here, $I_{\eta,max}$ is the motor current at maximum motor efficiency, $\omega_{m,\eta_{max}}$ is the motor turn rate at maximum motor efficiency and $Q_{m,\eta_{max}}$ is the motor torque at maximum motor efficiency.

Equation (18) indicates that to maximize efficiency resistance and no load current should be minimized while the supply voltage should be large. Due to unmodeled physics, it isn't quite that simple. For a single voltage the above is true, however, as seen in Figure **4** no load current is not constant and is approximately a linear function of supply voltage increasing with increasing voltage. The no load current comes from several sources including some electrical and mechanical losses which increase with motor turn rate and some electrical losses which are constant.

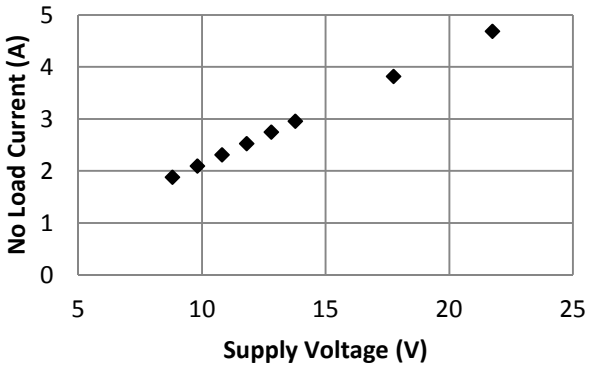

Figure 4. No load current vs voltage for a Neumotors 1935 1.5Y BLDC motor

Chapter 3 Propulsion System Design Methodology

The propellers used with small AUVs encounter several unique design challenges due to their small size and low turn rate. The first and largest challenge is that associated with low Reynolds number flow effects. Since the propellers are small and have limited rotational rate the sectional Reynolds number can be as low as 10,000. The limited size is due to the common desire to be of lower diameter than the AUV itself. The limited rotational rate comes from design for high efficiency. There are many losses in an AUV propulsion system and most of them scale with the propeller rotational rate.

Small propeller size also impacts manufacturing by making the complex geometry of the propeller more difficult to build. The propeller design may even call for features beyond the resolution of the manufacturing process. As a consequence the propeller design will need to accommodate the inherent limitations of whatever fabrication method is chosen.

3.1 Propeller Design

Propeller design is accomplished with a parametric design study in propeller diameter and turn rate. Each point in the parametric study is essentially a two-step process. First, given the required thrust, inflow velocity distribution, propeller diameter and propeller turn rate, OpenProp is used to determine the lift distribution corresponding to the minimum lift induced torque. Second, individual airfoil sections are designed along the span of the propeller blade in order to provide the required lift per unit span while minimizing drag per unit span. The two following sections describe these steps in more detail.

3.1.1 Minimum Induced Loss Lift Distribution

The lift distribution optimization performed by OpenProp follows the procedure described in Epps [21] which follows the work of Coney [15]. The problem is essentially to minimize the torque such that the required thrust is generated. According to lifting line theory, which makes use of blade element theory, the thrust and torque are given by,

$$T = Z \int_{r_h}^{R} [F_i \cos \mathrm{B}_i - F_v \sin \mathrm{B}_i] dr, \tag{21}$$

$$Q = Z \int_{r_h}^{R} [F_i \sin \mathrm{B}_i + F_v \cos \mathrm{B}_i] r dr, \tag{22}$$

Here, T is the propeller thrust, Q is the propeller torque, Z is the number of propeller blades, r_h is the propeller hub diameter, R is the propeller radius, F_i is the inviscid force generated at radial station r, F_v is the viscous force generated at radial station r, and B_i is the total incident velocity angle relative to the torque direction. The inviscid force is the lift force and the viscous force is the drag force.

Strictly speaking, lifting line theory does not predict a viscous force, but one can be added by introducing drag coefficients for the airfoil sections used.

The total incident velocity is the combination of velocity due to rotational motion, the ambient flow field and velocity induced by the propeller itself. For a given point in the parametric study the ambient flow

field and rotational motion are set, but the induced velocity is left free to vary. It is the induced velocity that is used to optimize the circulation distribution, and therefore lift distribution.

For more details on the optimization method see [15] and [21].

3.1.2 Airfoil Design

Airfoil design was attempted in a variety of ways including optimization and design space mapping. As was discussed in section 2.1.4, at low Reynolds number airfoil thickness is one of the most important parameters in determining performance. Since minimum thickness airfoils are desired, manufacturing limitations need to be considered.

3.1.2.1 Manufacturing Considerations and Impact

Manufacturing of propellers comes with a degree of difficulty because of the complex geometries involved. Additionally, the design level work for this project requires low-investment manufacturing since it is likely several design iterations will be required. There are a number of candidate manufacturing processes for propeller fabrication. Many of the processes can be categorized as those requiring molds and those not requiring molds.

Processes that utilize a mold often have a higher investment cost but much lower cost and time per part for high production numbers. This category includes processes like injection molding and investment casting.

Moldless processes will typically have a lower cost and time per part for low production numbers or prototypes. This includes precision CNC milled parts and rapid prototyped components. Between the two, rapid prototyped components while limited in material options are less costly and have a faster build time.

Given the prototyping nature of the project the best option then is rapid prototyping which includes 3D printing. 3D printing comes with resolution, surface finish, and structural limitations that will vary from one technology or material to another. The two main design limitations of using 3D printing based manufacturing are the minimum thickness and the stiffness of a blade.

Many of the airfoils designed for low Reynolds number flow have very low thickness to chord ratios particularly toward the trailing edge. Given the thickness limitation presented by 3D printing and the small overall propeller size the thickness to chord ratio is limited. Since low Reynolds number flow favors thin airfoils the thickness limitation may result in a constant thickness airfoil.

3.1.2.2 CFD Airfoil Optimization

The airfoil geometry design space was simplified by only investigating constant thickness airfoils with a seven point cubic spline based camber line.

The CFD software package Autodesk Simulation CFD 2014 360 was used with the laminar flow model. This software was chosen for two reasons, first it is freely available to university students with a three year license and second, because the 360 version of the software includes a cloud solving option. Cloud

solving allows the user to send multiple calculations to Autodesk's servers for simultaneous solving, a great tool for optimization tasks.

A substantial effort was successfully made to automate the optimization process linking together the optimization code from MATLAB, the CAD software used to generate geometries, Unigraphics NX8, and Autodesk Simulation CFD 2014 360. The result was an entirely hands-off optimization process using CFD as the plant model that took approximately one hour and fifteen minutes per iteration. Some difficulties were encountered.

Even with the entire process automated an hour and fifteen minutes per iteration was too slow. Determining the correct optimization parameters takes some trial and error resulting in a very large time commitment to get everything working properly. Additionally, airfoil performance has a significant bifurcation associated with stall. With additional time and effort these issues likely could have been overcome, but time constraints required the move to a faster design procedure. Figure **5** shows how a given geometry changed shape over several iterations using CFD.

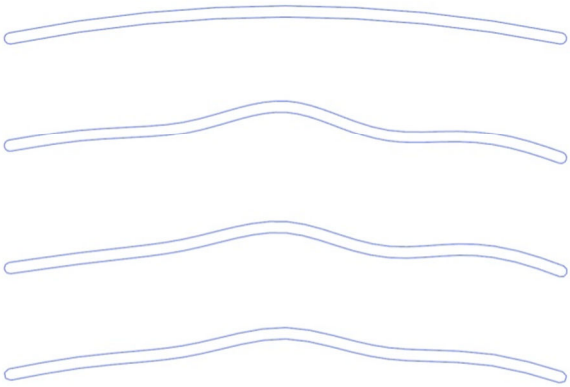

Figure 5. Sample geometry optimization results from 3 iterations of gradient ascent using CFD as a plant model.

3.1.2.3 XFOIL Airfoil Optimization

Moving on from CFD, it was decided to use a coupled viscous-inviscid flow solver as the plant model for optimization. Coupled viscous-inviscid flow solvers are very fast compared to CFD and XFOIL is a freely available, well studied example of such a solver. Once again, simple gradient ascent optimization was performed this time with XFOIL.

While using XFOIL dramatically sped up the process, it was discovered that gradient ascent was not a good optimization technique for the problem. The design space was filled with many local minima making it difficult to find an optimal design without using a very large number of initial design points. Ultimately the chosen solution was to reduce the design space by changing the geometry discretization and perform mapping instead of optimization.

3.1.2.4 XFOIL Design Space Mapping

Geometry discretization was simplified by continuing to design with a constant thickness and changing to a 3 point parabolic spline camber line. Since the leading and trailing edges were constrained to be

located at the points (0,0) and (1,0) the only two free geometry parameters were the maximum camber and the location of maximum camber.

The section thickness is defined by a constant thickness aft of 10% chord and forward of 90% chord. Section camber is defined by a parabolic spline camber line with the maximum camber and position of maximum camber defining the camber line. The thickness distribution is shown in Figure **6**. For x being the position along the airfoil chord, x_1 being the position of maximum camber, y being the amount of camber at a point and y_1 being the maximum camber, the camber spline is defined as,

$$\text{For, } a = 2 - 4x_1, b = 4x_1 - 1, c = 0, d = -4y_1, e = 4y_1, f = 0$$

$$s = \sqrt{\frac{x}{a} + \frac{b^2}{4a^2} - \frac{b}{2a}}, for\ x_1 < 0.5 \tag{23}$$

$$s = \sqrt{\frac{x}{a} + \frac{b^2}{4a^2} - \frac{b}{2a}}, otherwise$$

$$y = ds^2 + es. \tag{24}$$

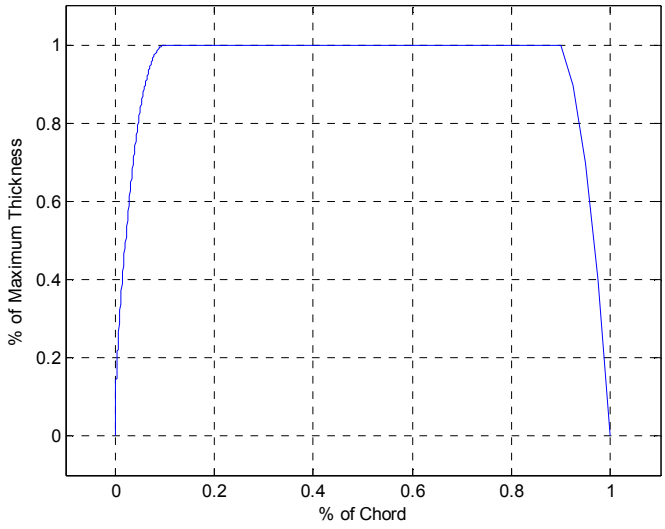

Figure 6. Airfoil thickness distribution

The design space was mapped by iterating over the parameters given in Table **1**.

Table 1. XFOIL design space mapping parameters.

Parameter	**Values**
Thickness/Chord	0.02, 0.04, 0.06, 0.08, 0.10, 0.12, 0.14
Maximum Camber/Chord	0.02, 0.03, 0.04, 0.05, 0.06, 0.07, 0.08, 0.09, 0.10
Position of Maximum Camber/Chord	0.3, 0.4, 0.5, 0.6, 0.7
Lift Coefficient Required	0.1, 0.2, 0.3, 0.4, 0.5, 0.6, 0.7, 0.8, 0.9, 1.0, 1.1, 1.2, 1.3
Reynolds Number x 10^{-3}	20, 40, 60, 80, 100, 125, 150, 200, 250

XFOIL allows the enforcement of a lift coefficient or an angle of attack when performing a calculation. Choosing a lift coefficient was done rather than an angle of attack because the ability to select an airfoil

section by lift coefficient is more useful than by angle of attack. The relationships between lift over drag, lift coefficient, chord and Reynolds number are easier to see than those with angle of attack in place of lift coefficient.

After mapping the design space a set of lookup tables was established relating the best performance and geometry to the input parameters: thickness over chord, lift coefficient required and Reynolds number. A couple example slices of the optimal lift over drag lookup table values are given in Figure **7**.

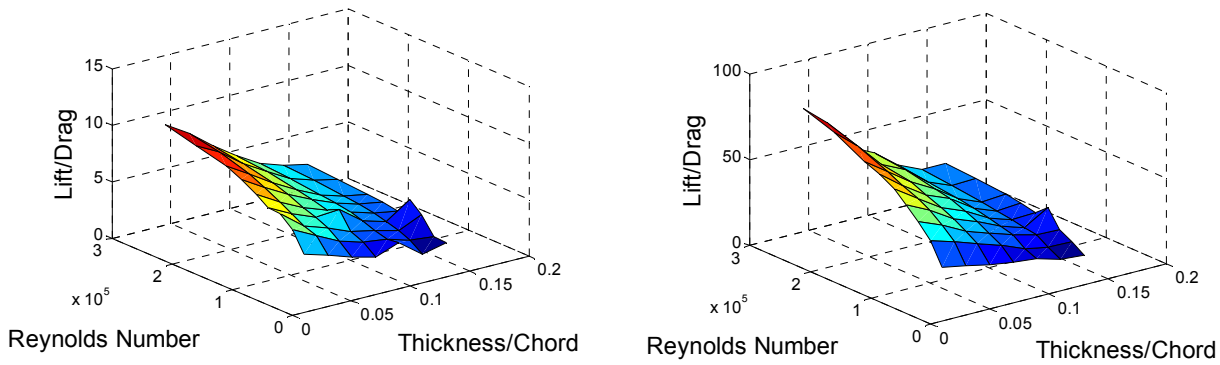

Figure 7. Example slices through optimal lift over drag mapping. The figure on the left is for a lift coefficient of 0.1 while the right is for 0.8. Results are consistent with low Reynolds number trends that best performance comes from high Reynolds number and low thickness.

3.1.2.5 Airfoil Selection

An individual airfoil section is selected in a parametric design study on lift coefficient. First, the lift per unit span required by the optimal lift distribution and minimum manufacturing thickness are used to determine the chord length and thickness over chord assuming a set of lift coefficients. The total velocity as determined by OpenProp is then used with the chord to determine the Reynolds number for each point in the parametric design study. The lookup tables are then used with three-dimensional linear interpolation to determine the best geometry and performance of each combination of thickness, Reynolds number, and lift coefficient. The lift coefficient with highest lift over drag and associated geometry is then chosen. An example of the resulting best lift over drag along a blade span versus input lift coefficient is given in Figure **8**.

XFOIL is used once again with the actual geometry, Reynolds number and angle of attack based on the lookup tables. This is to refine the three-dimensional interpolation estimate and get the best possible airfoil performance prediction.

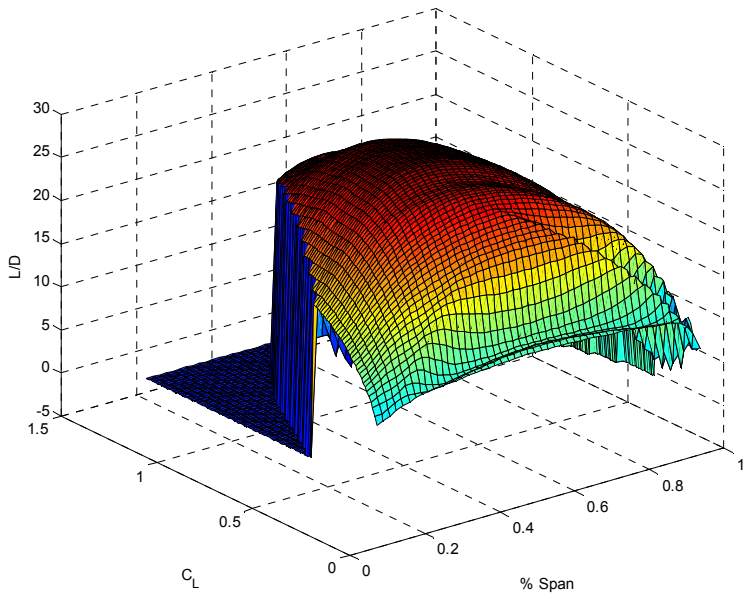

Figure 8. Example lift over drag versus radial station along the blade span and chosen lift coefficient. L/D is set to zero when the design point is outside of the mapped design space.

3.1.3 Propeller Analysis

At this point the propeller design is complete, but the propeller performance has not been predicted. The lift and drag coefficients as computed by XFOIL for each airfoil are numerically integrated over each blade using the total incident velocity on each section from OpenProp to estimate the total thrust and torque on the propeller as in equations (21) and (22) . Using these values the propeller constants K_T, K_Q and propeller efficiency are calculated at the design point. Off-design analysis can be done by using OpenProp to calculate the off-design total incident velocity and incident velocity angle at each section, using XFOIL to determine the lift and drag coefficients for each section and then numerically computing the thrust and torque on each propeller blade.

3.2 Motor and Battery Selection

The method of choosing a motor is straight forward. First, the motor requirements in terms of rotational rate and torque are determined. Next, the minimum operating voltage is determined; this will usually be set by systems other than the propulsion system. Using the minimum voltage and rotational rate the maximum motor constant required can be estimated. The K_V form, RPM/Volt, of the motor constant is almost always quoted with commercially available motors. A search of commercial-off-the-shelf motors is then performed for motors close to but not lower than the required motor constant K_V. Finally, of the motors found, the most efficient motor at the operating condition is chosen. The motor efficiency is determined using ideal motor theory.

3.3 Propulsion System Design Process Summary

A summary of the propulsion system design process is given below.

1. CFD is used to determine vehicle drag and flow velocity radial profile at the propeller location at the desired cruise velocity.
2. A parametric study on propeller turn rate and diameter is performed as follows:
    a. A propeller turn rate and diameter pair are chosen.
    b. OpenProp is used to determine the lift distribution corresponding to the minimum induced torque given the required thrust.
    c. At each radial station along the propeller blade where the lift distribution is defined:
        i. A range of lift coefficients from 0.1 to 1.3 is chosen.
        ii. For each lift coefficient a specific chord is calculated using the OpenProp-determined section lift and incident velocity according to the section lift equation, $l_{req} = \frac{1}{2}\rho V^2 C_l c$.
        iii. For each lift coefficient, using the chord and incident flow velocity the Reynolds number is determined.
        iv. For each lift coefficient, the thickness to chord ratio is determined by dividing the minimum manufacturable thickness by the chord.
        v. For each lift coefficient, the optimal lift over drag and associated geometry is determined using the lookup tables referenced in 3.1.2.4 as a function of lift coefficient, Reynolds number and thickness to chord.

vi. The best lift over drag for the entire lift coefficient range is then used to select the lift coefficient and associated geometry.

d. Once the geometry and lift coefficient is determined for each radial station a parabolic least squares fit on lift coefficient is determined to smooth the lift coefficient distribution and as a result also smooth the chord distribution.
e. For each radial station and using XFOIL, given the geometry from the lookup table and the newly smoothed lift coefficient and resulting thickness over chord and Reynolds number, the required angle of attack and drag coefficients are calculated.
f. Using blade element theory, the elemental thrust and torque from each radial station is then calculated and integrated to determine the total thrust and torque on the propeller (the thrust will be the required thrust).
g. Propeller efficiency is calculated by $\frac{P_{out}}{P_{in}}$ where $P_{out} = V_A T$ and $P_{in} = Q\omega$.
h. The propeller design is checked for cavitation using tools build into OpenProp and if cavitation is detected the lift coefficient distribution is altered to reduce the lift at sections near the blade tip.

3. Candidate propeller designs are chosen based on the results of the parametric study.
4. The minimum possible battery voltage for the vehicle system determined.
5. For each of the candidate propeller designs:
    a. The approximate motor constant in the K_V form is determined by dividing the required propeller turn rate by the minimum possible battery voltage.
    b. A search for BLDC motors with K_V constant near and above the approximate value is performed.
    c. Using the three constant motor model and whatever additional motor loads will be present (seals, oil, bearings, etc.) the performance and required motor/effective voltage of each of the found motors is determined.
    d. The duty cycle of each motor is determined for battery configurations starting at the minimum possible voltage and up to several additional battery series cells.
    e. A motor is chosen based on predicted total system efficiency, maximizing the duty cycle at minimum voltage and minimum motor size/weight.
6. The final propulsion system is determined by comparing the total system efficiency and size/weight of each of the candidate propeller designs and associated motor selections.

Chapter 4 Propulsion System Analysis and Design

Two new propulsion systems were designed for the 690. The first is simply a new propeller based on low Reynolds number section data in [19]. The purpose of the first design is to experiment with manufacturing techniques and show that a propeller appropriately designed for low Reynolds number flow has better performance and that performance can be better predicted. The second is an entirely new propulsion system design possibly including new battery voltage, motor and propeller.

First, however, it is instructional to analyze and identify the flaws of the original propulsion system.

4.1 Original Propulsion System

The original 690 propulsion system was actually intended for use with the Self-Mooring AUV. The Self-Mooring AUV has common features with the 690, however, the 690 has higher drag and doesn't have some of the battery requirements of the Self-Mooring AUV.

This section will analyze the original propulsion system as it performed in the 690 with new performance predictions based on the current design process.

4.1.1 Propeller Analysis Results and Discussion

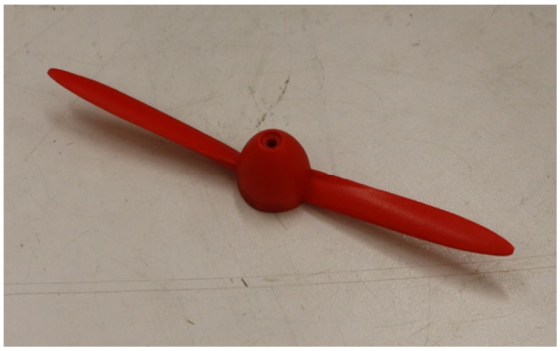

Figure 9. Original propeller

Since the original propulsion system was designed for a different thrust requirement the associated propeller performance first needs to be adjusted to the 690 requirements. The Self-Mooring AUV propulsion system requirements are listed in the table below.

Table 2. Self-Mooring AUV Propeller Design Parameters

Parameter	Value
Thrust (N)	8.67
Cruise Speed (m/s)	2.00
Turn Rate (rpm)	1850
Advance Ratio (dimensionless)	0.5405

The 690 AUV requires a cruise speed of 2 m/s, however, at this velocity the thrust required according to CFD is 10.21 N. The equations relating thrust, turn rate and torque are,

$$T = \rho D_p^4 n^2 K_T(J), \tag{25}$$

$$K = \rho D_p^5 n^2 K_Q(J). \tag{26}$$

As a reminder, here T is the propeller thrust, ρ is the fluid density, D_p is the propeller diameter, n is the propeller turn rate in rotations per second, $K_T(J)$ is the thrust coefficient as a function of advance ratio, J, and $K_Q(J)$ is the torque coefficient as a function of advance ratio.

The thrust and torque coefficients, K_T and K_Q, of the original propeller were found using OpenProp and given along with efficiency in the figure below.

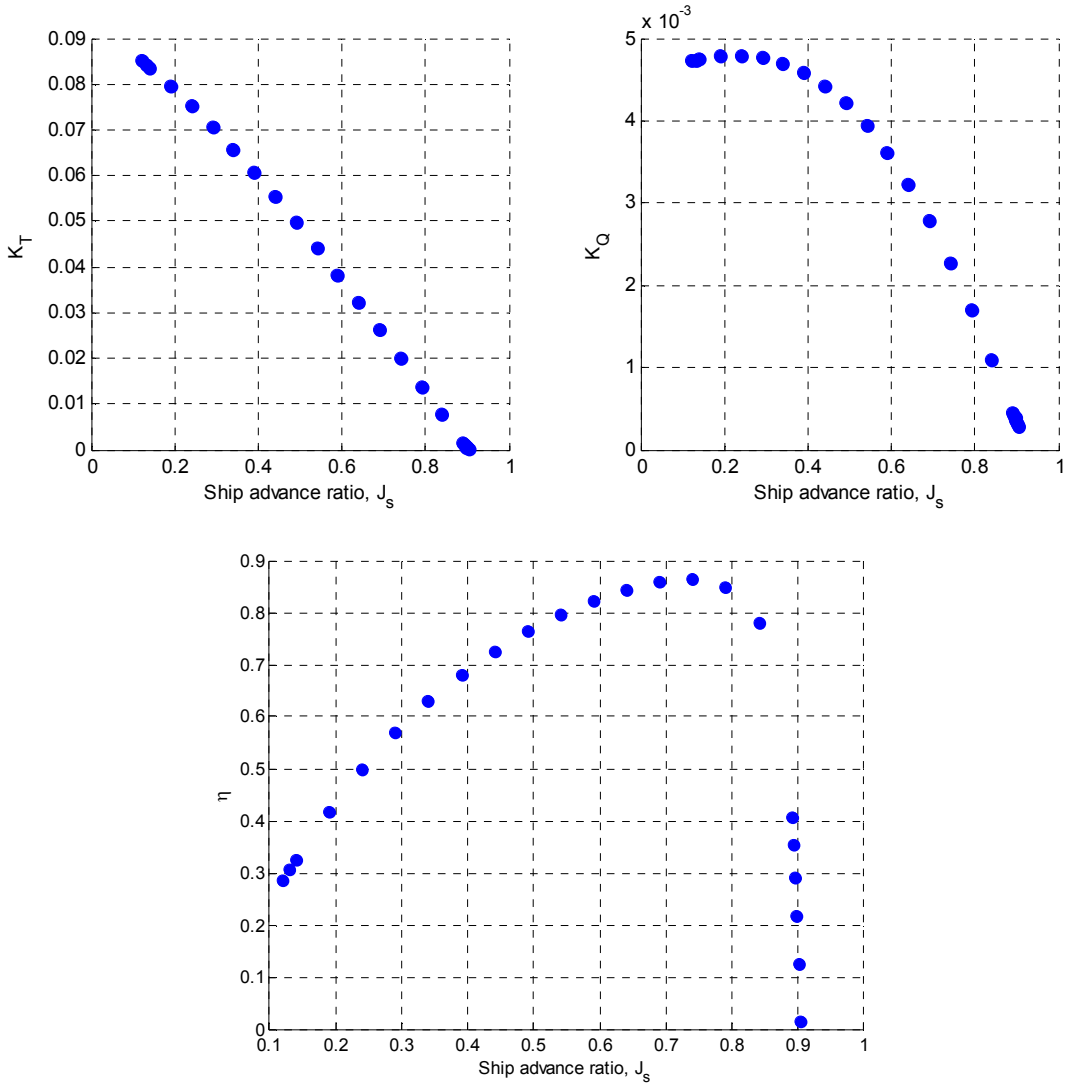

Figure 10. Self-Mooring AUV propeller performance curves.

If the advance coefficient, J, is assumed to remain constant for the new thrust requirement then K_T also stays the same and the turn rate, n, is solved for as 33.5 RPS. However, this new turn rate and the same forward velocity result in a new advance ratio of 0.497. By iterating through this process the turn rate and advance ratio will eventually converge on a new pair of values. For this particular case they are a turn rate of 32.42 RPS (1945.2 RPM) and advance ratio of 0.5141 corresponding to a thrust coefficient of 0.0459, torque coefficient of 0.00397 and efficiency of 78.17%.

According to the old design and analysis methodologies the task to determine the new required turn rate would be complete; however, according to the new approach we should evaluate each of the airfoil sections along the blade. Figure **11** shows the section lift coefficient for the original propeller as determined by both OpenProp and XFOIL.

OpenProp chooses section lift coefficients and determines geometry to match them. The geometry is set to match the section lift coefficient by first choosing one of several generic sectional geometries. The generic sectional geometry will have a single combination of lift coefficient, angle of attack and camber. To achieve different lift coefficients the angle of attack and maximum camber are scaled linearly with the lift coefficient.

Beyond Figure **11** is Table **3** with the overall properties of the propeller according to OpenProp and XFOIL. In Table **3**, propeller efficiency is the inflow adjusted efficiency,

$$\eta_A = \frac{TV_A}{2\pi Qn}. \tag{27}$$

Here, η_A is the inflow adjusted efficiency, T is the thrust, V_A is the inflow adjusted velocity, Q is the toque and n is the propeller turn rate in rotations per second.

The inflow adjusted efficiency uses the inflow adjusted velocity in place of the ship velocity. Since the propeller sits in the AUV wake the flow velocity at the propeller is lower than the ship velocity resulting in the propeller producing less power. This is opposed to the open water efficiency which would assume the propeller experiences flow speed equal to the ship speed.

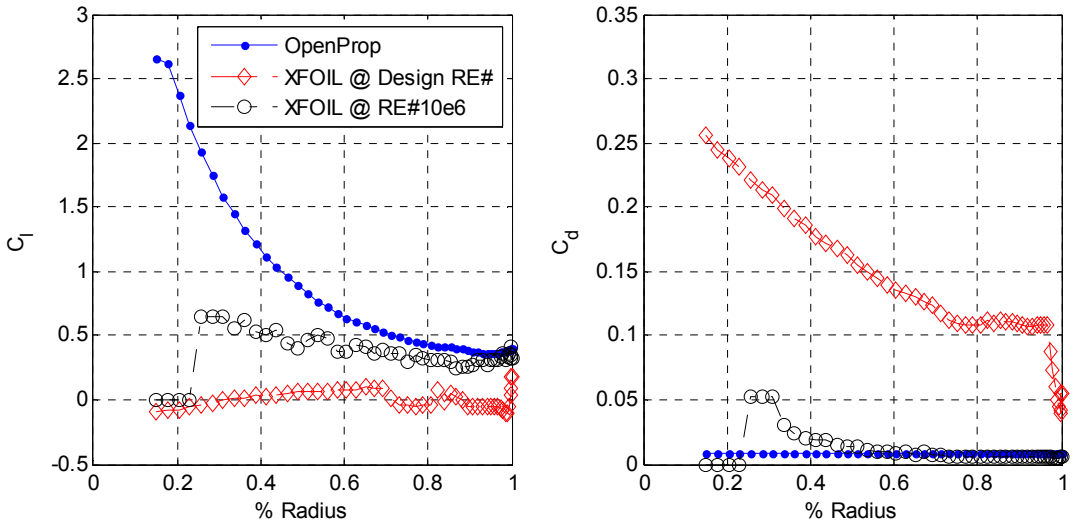

Figure 11. Radial distribution of lift and drag coefficient for the original 690 propeller as determined by OpenProp and XFOIL

In Figure **11**, and hereafter, the design Reynolds number is the Reynolds number resulting from the designed turn rate, incident velocity and section chord length. Figure **12** gives the design Reynolds number distribution for the original propeller design.

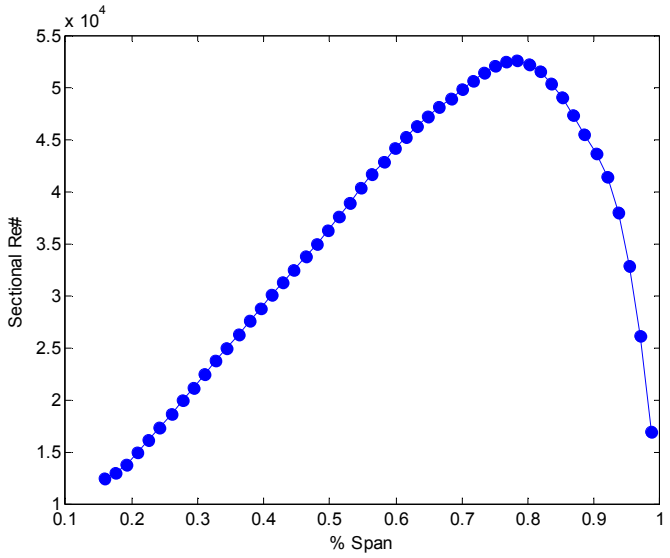

Figure 12. Reynolds number versus radial location for the original propeller design.

Results referred to as 'OpenProp results' and 'XFOIL results' are calculated using the same blade element theory approach and only differ in how the lift and drag coefficients along the span are calculated. If the two methods happened to have the same lift and drag coefficients the predicted thrust and torque would be identical.

Table 3. Predicted performance comparison of the original 690 propeller.

Parameter	**OpenProp**	**XFOIL Design Re**	**XFOIL Re = 10e6**
Thrust (N)	10.21	-0.4245	7.005
Torque (N-m)	0.1060	0.1027	0.0765
Efficiency (%)	78.17	-3.36	74.48
Max Section Lift Coefficient	2.5699	0.1771	0.6413
Max Section Drag Coefficient	0.0080	0.2558	0.0520

XFOIL reporting negative thrust at the design Reynolds number suggests that, either the design is bad, or that XFOIL isn't a great tool for this purpose. The propeller has demonstrated experimentally that it produces positive thrust. This suggests XFOIL is the problem. The XFOIL determined pressure distribution over the airfoil section at 70% span is given in Figure **13**. The pressure distribution has a nearly constant value from approximately the midchord to the trailing edge. This is indicative of large scale separation. A further investigation of results from XFOIL shows that the boundary layer properties also indicate large scale separation over most of the blade.

XFOIL is a tool designed to handle thin regions of separation, such as laminar separation bubbles, but isn't capable of accurately modeling large scale separation as in this case. The unusually high thickness of the propeller blade, generally above 20% chord, is the likely source of the low Reynolds number separation.

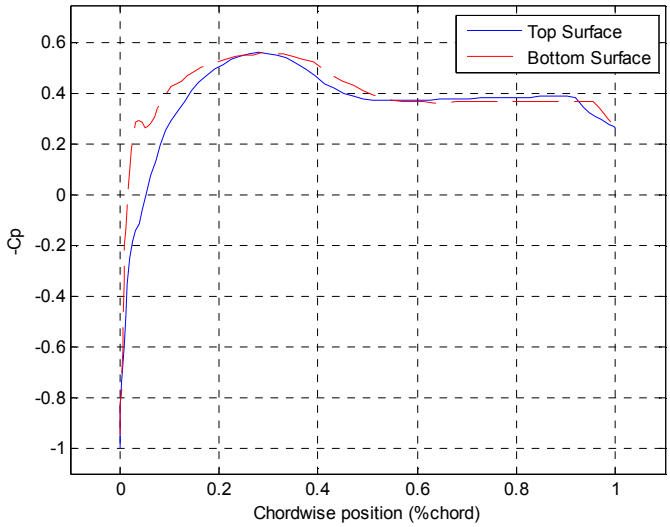

Figure 13. XFOIL pressure distribution at design Reynolds number at 75% span.

Figure **11** and Table **3** also give results for a high Reynolds number calculation. The high Reynolds number calculation was done for two reasons: first, as a sanity-check that all of the associated code was functioning properly; and second, to show how higher Reynolds number flow results in performance with better, although still not great, agreement with the OpenProp prediction. The high Reynolds number calculation essentially predicts the performance if the propeller boundary layer is completely turbulent.

The reader may also wonder why the torque reported in Table **3** for the OpenProp results and the design Reynolds number XFOIL results are so similar when the section drag coefficients are so much larger for XFOIL in Figure **11**. The answer is that the contribution to torque by lift for the OpenProp results accounts for over 90% of the total torque while for the design Reynolds number XFOIL results the torque due to drag accounts for over 90% of the total torque.

Finally, Figure **14** gives the performance curves of the original propeller as determined by OpenProp, XFOIL at the designed operating condition, and XFOIL at a Reynolds number of ten million. The efficiency shown is set to zero for any torque or thrust coefficients of the incorrect sign. From Figure **14** it could be concluded that the predicted separation at low Reynolds number renders XFOIL incapable of determining performance and that at high Reynolds number XFOIL results are still very different from the OpenProp results. The difference between the two can largely be attributed to OpenProp overestimating the maximum lift coefficient and a lower viscous drag calculated by XFOIL.

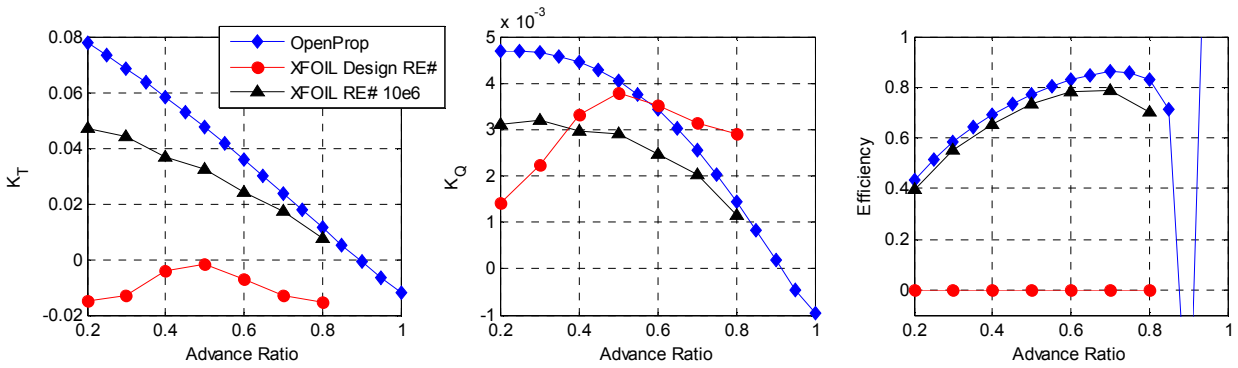

Figure 14. Thrust coefficient, torque coefficient and efficiency as determined by OpenProp and XFOIL. XFOIL data represents both the 2 m/s forward velocity condition and a high Reynolds number case representing turbulent flow.

4.1.2 Motor and Other System Losses

The motor used in the original propulsion system is a Neumotors 1925/3Y brushless DC motor. The manufacturer supplied and experimentally confirmed specifications of this motor are given in Table **4**.

Table 4. Neumotors -1925/3Y motor constants.

Parameter	Value
K_V (RPM/V)	136
K_Q (in-oz/A)	9.94
Motor Resistance (ohm)	0.18
No Load Current (A)	0.3

Loads on the motor in additional to the propeller are due to the pressure-compensated motor housing. The housing adds loads via the friction with the oil with which it is filled, bearing losses and rotary lip seal losses. The losses due to oil were investigated by Duelley [11], finding that the no-load current was essentially increased by 0.322 Amps which corresponded to 1.11 oz-in for the motor in use. Bearing losses are assumed to be negligible and rotary seal testing by this author determined a nearly constant with turn rate additional torque of 1.5 oz-in.

4.1.3 Predicted Performance

The entire system performance is determined by working from the propeller to the battery. First, it should be noted that the majority of 690 testing has been performed with a temporary battery pack having a nominal operating voltage of 25.5 V. Therefore, this prediction will assume a 25.5 V supply voltage.

The propeller turn rate and torque required to generate the 10.21 N of thrust required for cruise at 2 m/s can be calculated from the performance curves of section 4.1.1. OpenProp based analysis results in a required turn rate and torque of 1942 RPM and 0.1060 N-m. The low Reynolds number XFOIL analysis yields no results due to predicted separation. The high Reynolds number XFOIL analysis yields a required turn rate and torque of 2231 RPM and 0.1037 N-m. These requirements are also given in Table **5**.

Table 5. Original propulsion system propeller rates and loads

Parameter	Value, OpenProp	Value, XFOIL
Propeller Turn rate (RPM)	1942	2231
Propeller Torque (N-m)	0.1060	0.1037

The propeller requirements are then combined with the extra loading due to the seals and oil to determine the requirements on the motor. The required effective voltage and current is then calculated. All of these calculations can be easily set up in a spreadsheet. The values are given in Table **6**.

Table 6. Original propulsion system motor calculations.

Parameter	Value, OpenProp	Value, XFOIL
Motor Turn Rate (RPM)	1942	2231
Motor Torque (N-m)	0.1166	0.1143
Motor No-load Current (A)	0.322	0.322
Required Current (A)	2.28	2.25
Required Voltage (V)	14.69	16.82

The required current is then divided by the motor controller efficiency. The motor controller efficiency is assumed to be 97%. The motor controller effective duty cycle is given by,

$$DC_{eff} = \frac{n}{K_V(V_m - I\,R_S)}. \tag{28}$$

This gives an effective duty cycle of 55.7% and 63.96% for the OpenProp and XFOIL predicted performance, respectively. An ideal motor controller can be modeled as transforming the supply voltage and current to the motor voltage and current by,

$$V_m = V_s\,DC_{eff}, \tag{29}$$

$$I_m = \frac{I_s}{DC_{eff}}\eta_{mc}. \tag{30}$$

Here, V_m is the motor voltage, V_S is the battery supply voltage, I_m is the motor current, I_S is the battery supply current, and η_{mc} is the motor controller efficiency.

From (20), the battery current is 1.31 A for OpenProp and 1.48 A for XFOIL.

This results in a total system power requirement of 33.4 W for the OpenProp prediction and 37.8 W for the XFOIL prediction. The effective power output is the vehicle drag multiplied by the vehicle velocity, giving 20.4 W. The overall power efficiency is then 61.1% for the OpenProp prediction and 54.0% for the XFOIL prediction. These predictions are summarized in Table **7**.

Table 7. Overall original propulsion system performance prediction summary.

Parameter	Value, OpenProp	Value, High Reynolds number XFOIL
Input Power (Watts)	33.4	37.8
Output Power (Watts)	20.4	20.4
Efficiency (%)	61.1	54.0

4.1.4 Experimental Results

The 690 was tested in Claytor Lake to determine propulsive performance. The 690 testing mission profile consisted of the vehicle diving and then being given 30 seconds to achieve steady state flight at a depth of 2 m and constant heading followed by a series of changes in commanded motor turn rate each with an additional 20 seconds to achieve steady state.

Data reduction following field tests shows that the required propeller turn rate to achieve 2 m/s flight is higher than predicted. Figure **15** shows the relationship between propeller turn rate and forward velocity as measured by the 690 Doppler Velocity Logger (DVL). From Figure **15** the propeller turn rate required for 2 m/s flight is approximately 2600 RPM. This corresponds to an advance ratio of 0.385.

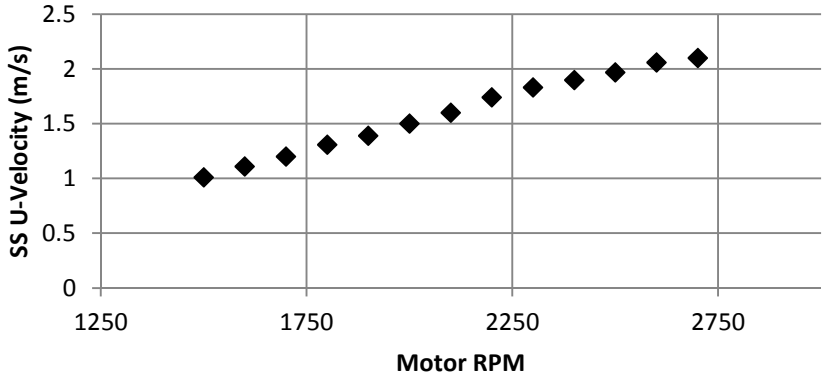

Figure 15. Experimental steady state forward velocity vs motor turn rate for the original 690 propulsion system.

If the propeller performance as predicted by OpenProp and XFOIL hydrodynamic coefficients are taken to be correct this corresponds to a drag/thrust of 24.0 N and 15.2 N and torque of 0.2152 N-m and 0.1441 N-m, from the OpenProp and XFOIL analyses respectively.

If ideal motor theory and the motor constants defined in Table **4** and Table **5** are assumed to be correct, then the torque required by the propeller can be calculated from the current delivered to the motor. According to the experiment data logs the average supply voltage and current at 2600 RPM were 23.8 V and 3.24 A. Next by multiplying the supply power by the assumed motor controller efficiency the power into the motor is found as 74.8 W.

According to equation (14) in section 2.2.2, for a given motor, load and motor turn rate a specific voltage, call it the effective or motor voltage, is required. The voltage supplied by the system battery is likely higher than the effective voltage. The motor controller used with the motor takes care of this by reducing the effective voltage on the motor windings at some cost to efficiency. The relationships between battery current and voltage, motor controller efficiency and duty cycle and motor current and voltage are given in equations (28), (29), and (30).

Given the requirements on the motor the effective voltage at 2600 RPM is 19.52 V. Using the power into the motor this means the effective current is 3.832 A. Subtracting the no-load current and then multiplying by motor K_Q, the torque is found to be 0.2253 N-m. By removing the 1.5 oz-in due to the seal and 1.1 oz-in due to oil the propeller drive torque is 0.2147 N-m. This process of calculating the

propeller drive torque is given by Equation (31). At the operating point this corresponds to thrust and torque coefficients of 0.0256 and 0.0045, respectively. The propulsion system efficiency is then computed as vehicle power out over electrical power in, giving 26.5%. All of these results are summarized in Table **8**.

$$Q_p = K_{Q,m}\left(\eta_{mc}\frac{I_s}{DC_{eff}} - I_{nl}\right) - Q_s. \tag{31}$$

Here, Q_P is the propeller torque, $K_{Q,m}$ is the motor torque constant, and Q_S is the torque associated with the seal, oil and other loads in the motor housing.

Table 8. Original propulsion system propeller and complete propulsion system values assuming different models correct

	Value Assuming Correct		
Parameter	OpenProp	High Reynolds # XFOIL	CFD (for drag) & Motor Theory
K_T	0.0601	0.0380	0.0256
K_Q	0.0045	0.0030	0.0047
Prop Efficiency (%)	67.7	63.8	27.6
Thrust (N)	24.0	15.2	10.21
Torque (N-m)	0.2152	0.1441	0.2253
System Efficiency (%)	61.1	54.0	26.5

4.1.5 Discussion and Conclusions

From the information in sections 4.1.1 to 4.1.4 several conclusions can be reached about the original propulsion system and analysis methods.

1. High thickness to chord ratio foils operating at low Reynolds number will cause XFOIL to fail. This is because of the high likelihood of large scale separation, something XFOIL is incapable of modeling correctly.
2. The design lift coefficients near the root of the original propeller are far higher than are realistically possible. OpenProp makes section adjustments using thin airfoil theory which assumes there is no maximum lift coefficient.
3. Even at very high Reynolds numbers, XFOIL predicts a cap on the lift coefficient likely resulting in a more accurate predicted lift.
4. The propeller efficiency calculated using motor theory being so much lower than the efficiency from either the OpenProp or the high Reynolds number XFOIL analyses may be due to a combination of factors.
    a. The first that may be suspected is that the no-propeller-load condition current load is larger than represented. Measurements taken using the 690 without the propeller in place suggest the total no-propeller current at 2600 RPM is 0.5840 A, which is actually smaller than the 0.622 A arrived at by adding current due to the seal and oil torque to the motor no-load current. This implies there is no unmodeled loading.
    b. It is possible that the torque coefficient of the motor is incorrect. A five percent change of K_v from 136 to 143 results in a K_Q of 0.0668 and torque of 0.2141. This would change

the propeller torque coefficient to 0.0045 and efficiency to 28.9%. While the difference is not inconsequential, it suggests the motor torque coefficient would have to be very incorrect to account for the approximately 40% difference in propeller efficiency.

c. The final option is that the high Reynolds number drag coefficients calculated by XFOIL are not appropriate for this application. The viscous forces may be very important to this particular problem and a high Reynolds number drag coefficient is too small. The drag coefficients in OpenProp are chosen by the user and not justified unless the user justifies them externally. This suggests it is important to capture the low Reynolds number effects.

4.2 Propeller Only Redesign

As stated previously, the main intention with this design was to experiment with propeller manufacturing and produce a more suitable geometry for low Reynolds number flow. With a more suitable geometry performance prediction is expected to improve.

4.2.1 Propeller

The foil section of interest discussed in [19] is a 5% camber wing with 1.4% thickness to chord and an aspect ratio of 6. The lift and drag coefficient data for this section was incorporated into the propeller design in place of using the optimal airfoil section lookup tables and setting the section chord to avoid cavitation. Unfortunately, the lift curve in [19] was given versus the angle of attack relative to the no-lift angle of attack without the no-lift angle of attack being given. The no-lift angle of attack was estimated using the thin airfoil theory solution for a parabolic camber line, as given in section 2.1.1.2. This analysis gave a no-lift angle of -5.2 degrees. A 1.4% thick airfoil is extremely thin for the small scale of the propeller. As such, this propeller design ignores the thickness simply trying to minimize it.

A couple of changes were also made to the base parameters of the propeller design. The design propeller turn rate was changed to 2000 RPM because that is in the midrange of the motor currently in the 690. The propeller was also designed to be slightly smaller in diameter, 0.10 m, and 3-bladed to aid performance in diving. It was thought a smaller diameter and larger number of blades would result in a more consistent propulsive force while on the surface. A more exhaustive design process could have been attempted looking at a wider variety of diameters, blade numbers and turn rate, but given the purpose of this redesign it was deemed unnecessary.

The propeller was designed in a manner similar to that described in section 3.1. First the lift distribution was determined using the minimum induced loss optimizer from OpenProp. The lift coefficient distribution over the blade span was then set to provide a smooth chord distribution. The lift coefficient distribution was varied over several iterations to improve efficiency. Next, experimental data from [19] was used to determine the required angle of attack and resulting drag coefficient distributions for the previously described airfoil section and lift coefficient distribution.

The predicted performance curves of the propeller are given in Figure **16**. Since the design point has turn rate of 2000 RPM and forward velocity of 2 m/s the advance ratio is 0.6. The data shown in Figure **16** is for performance prediction based on section coefficients from the Laitone data, section

coefficients from an XFOIL calculation at the design Reynolds number and low inflow turbulence (~0.070% turbulence level), an XFOIL calculation at high Reynolds number and an XFOIL calculation at the design Reynolds number and high inflow turbulence (~2.00% turbulence level).

The performance curves show some unexpected results. With the propeller designed based on experimental data collected at a Reynolds number of 20,700 the low Reynolds number XFOIL analysis results should have better agreement with the Laitone-based results. The high turbulence prediction has better agreement with the Laitone-based results than does the low turbulence prediction, but still is not very good. Table **9** gives the predicted thrust and torque at the design point for the various prediction methods. Given the seemingly poor results a further analysis of the airfoil performance is warranted.

Table 9. Propeller performance values at the design point, 2 m/s flight at 2000 RPM turn rate as determined using different lift and drag coefficient sources.

Parameter	**Laitone Data** [19]	**XFOIL Design Re#**	**XFOIL Re# 10e6**	**XFOIL Design Re# High Turbulence**
Thrust (N)	10.21	-7.371	6.817	1.9138
Torque (N-m)	0.1447	-0.0047	0.0732	0.0557
Efficiency (%)	53.0	0	69.2	25.8
Max Section Lift Coefficient	0.7887	0.3522	0.8509	0.5801
Max Section Drag Coefficient	0.0735	0.0826	0.00829	0.0681

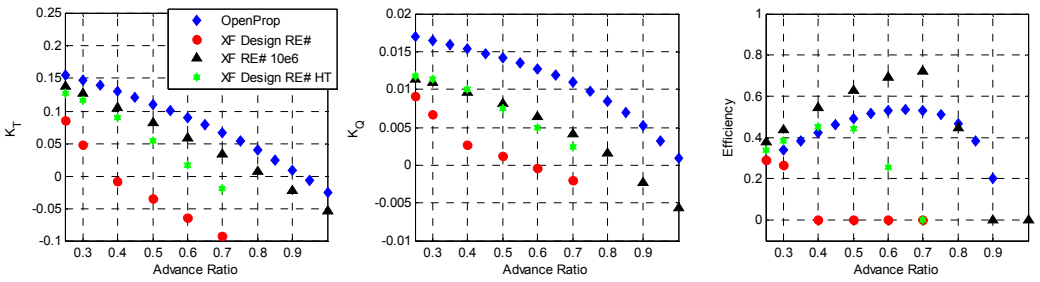

Figure 16. Initial propeller redesign performance curves from different analysis methods. For the design Reynolds number case, the forward velocity was held constant at 2 m/s and the propeller turn rate varied to give different advance ratios. This means the Reynolds numbers also changed for the design Reynolds number case.

4.2.2 Propeller Airfoil Analysis

Figure **17** shows a comparison of the sectional lift and drag coefficient distribution over the propeller span for the new propeller as determined by XFOIL and the Laitone data. As before, the Laitone results are those calculated with the zero-lift angle of attack determined by thin airfoil theory (-5.2 degrees). The calculated angle of attack for all four cases is the same because all four cases have the same geometry and predicted flow incident velocity direction. Angle of attack is determined by comparing the pitch angle of the airfoil section to the incident velocity direction as determined by OpenProp.

Since the angle of attack is the same the derivative of the lift coefficient with respect to span is approximately the lift curve slope ($\frac{dC_l}{d\alpha}$) with some spanwise varying, but common to all cases, multiplicative factor. The lift vs. span curves appear to match fairly well in slope but have an offset between the design Reynolds number XFOIL results and those from Laitone. This suggests that the zero-lift angle of attack as determined by thin airfoil theory is incorrect.

Since thin airfoil theory assumes inviscid flow, this isn't shocking and should have been anticipated. This implies the propeller as designed will not be very effective. Especially interesting about Figure **17** is that the high Reynolds number XFOIL calculation predicts the section lift coefficients fairly well, while the low Reynolds number XFOIL calculations predict the section drag coefficients better. The high turbulence low/design Reynolds number XFOIL calculation appears to be the best of both with better lift coefficient agreement than the low turbulence low/design Reynolds number XFOIL calculation and better drag coefficient agreement than the high Reynolds number XFOIL calculation. The difference between the section drag coefficient of the design XFOIL results and the Laitone values near the propeller tip may be explained by the rapidly increasing thickness to chord ratio near the tip. An increasing drag coefficient with increasing thickness to chord ratio is consistent with low Reynolds number airfoil trends.

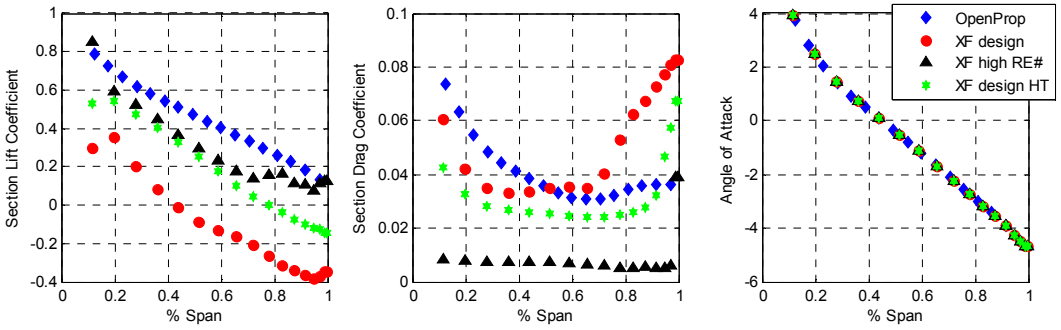

Figure 17. Section lift coefficient distribution by different methods. The OpenProp numbers are based on the data presented in Laitone, XF design are the XFOIL design Reynolds number low turbulence values, XF high RE# are the XFOIL high Reynolds number values and XF design HT are the XFOIL design Reynolds number and high turbulence values.

Figure **18** illustrates the difference between the lift curve from [19] and low/design Reynolds number XFOIL. The data from Laitone is wind tunnel data from a wing section and will have a slightly lower lift curve slope as a result. Since the Laitone curve has a different slope due to three dimensional effects, the curves appear to match up rather well with an offset. The n-value given in the figure is the linear stability theory amplification factor and corresponds to the inflow turbulence level; n = 9 corresponds to a 0.070% turbulence level and n = 0.95 corresponds to a 2.00% turbulence level. This suggests that airfoil design should be done at the design Reynolds number with a high turbulence level when tunnel data is not available.

Figure **19** shows the lift and drag curves when the no-lift angle of attack for the Laitone data is determined using XFOIL (approximately -1.5 degrees) instead of thin airfoil theory. While the lift curve is still fairly different due to finite wing effects, the drag curve has very good agreement for the low Reynolds number, low turbulence case.

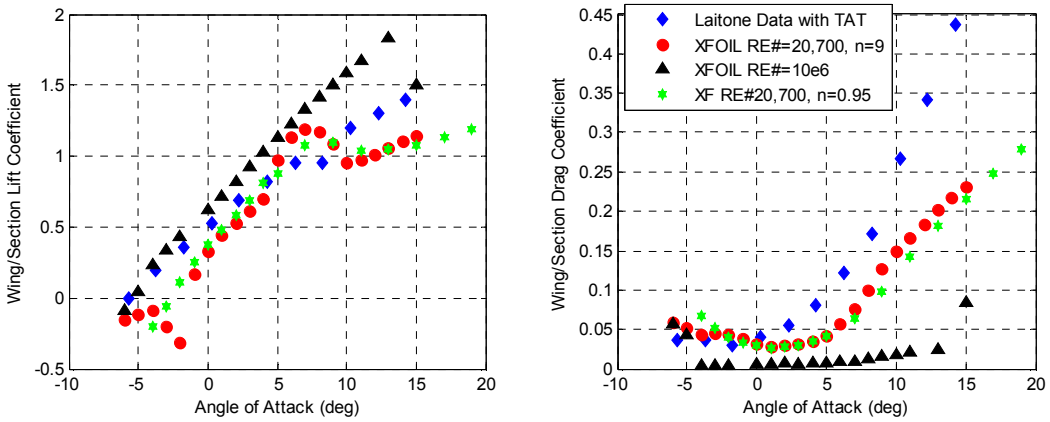

Figure 18. XFOIL and Laitone wind tunnel data for lift and drag coefficients. The XFOIL data is section data while the Laitone data is wing data with the zero lift angle of attack determined by thin airfoil theory.

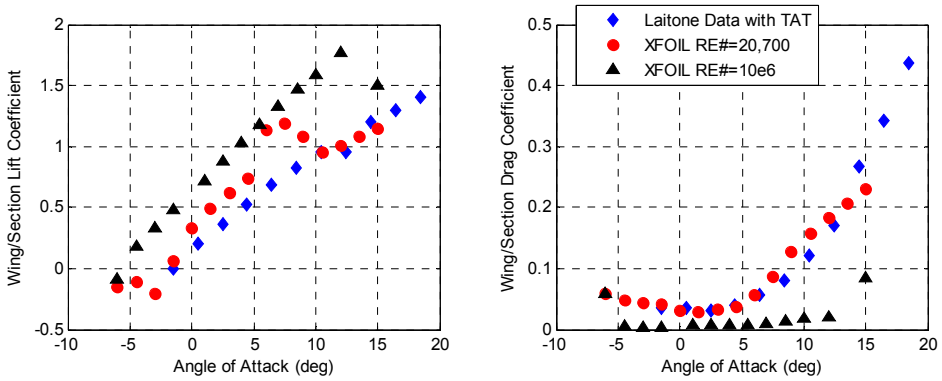

Figure 19. XFOIL vs Laitone data with a 4.2 degree offset in the Laitone angle of attack to match the low Reynolds number XFOIL no-lift angle of attack. This offset represents a correction to the zero-lift angle of attack as calculated by thin airfoil theory.

4.2.3 Propeller Manufacturing

With a propeller design in hand, manufacturing processes were the next thing to investigate. Before propeller designs were sent out for fabrication, files of the proper format needed to be created. Unfortunately, propellers generally have a complex geometry and are not easy to generate in CAD software. Ultimately, the solution was writing an enhancement to OpenProp to allow the direct export of stereolithography (STL) and Initial Graphics Exchange Specification (IGES) files. Such files can then be imported to most CAD software and the specific hub geometry added.

Propellers were constructed using a variety of processes. 3D printing in some form or another was used in all of them.

Fused deposition modeling (FDM) printing was used to produce extremely inexpensive propellers, but would have required much higher thicknesses to attain the necessary stiffness. It was initially expected that FDM propellers would be too rough due to build lines, but with manufacturer provided polishing the roughness was acceptable.

Figure 20. FDM propeller

PolyJet printing was used to make more expensive propellers with higher stiffness, higher build resolution and a smoother final part. Like the FDM propellers, the PolyJet propellers were not stiff enough on their own. The stiffness of the PolyJet propellers was enhanced via electroplating with a nickel-copper alloy with great success. These plated PolyJet propellers were those used in testing.

Figure 21. PolyJet and plated polyJet propeller

A pair of bronze propellers was also manufactured at lower total cost than the plated propellers. The manufacturing process includes 3D printing in wax, followed by the production of a plaster mold and then casting of parts. The resulting propellers looked excellent but had obvious geometry defects, likely from handling while still only wax models. The propeller geometry attempted was at the very edge of what the manufacturer claimed may be possible so it is not surprising there was a failure. While the bronze cast propellers were not used beyond this point, the process bears further investigation; small changes to the geometry may result in the process being reliable and eventually lower cost than that of the plated propellers.

Figure 22. Cast bronze propellers

4.2.4 Predicted Performance

Using the performance curves in Figure **16** the propeller turn rate and torque to produce the required thrust at required vehicle speed are given in Table **10**.

Table 10. Propeller redesign speed and torque requirements

Parameter	Laitone Data	XFOIL Design Reynolds number	XFOIL High Reynolds number	XFOIL Design RE# High Turbulence
Propeller Turn rate (RPM)	2000	3447	2187	2474
Propeller Torque (N-m)	0.1447	0.1913	0.1045	0.1372
Propeller Efficiency (%)	53.0	13.9	66.0	44.4

Combining the seal torque, and motor constants result in motor requirements given in Table **11**.

Table 11. Redesigned propeller motor requirements.

Parameter	Laitone Data	XFOIL Design Reynolds number	XFOIL High Reynolds number	XFOIL Design RE# High Turbulence
Motor Turn Rate (RPM)	2000	3447	2187	2474
Motor Torque (N-m)	0.1630	0.2097	0.1229	0.1556
Motor Current (A)	2.622	3.286	2.050	2.515
Motor/Effective Voltage (V)	15.1	25.75	16.48	18.67

Using a motor controller efficiency of 97% the power and efficiency predictions are given in Table **12**.

Table 12. Predicted power and efficiency of the new propeller propulsion system.

Parameter	Laitone Data	XFOIL Design Reynolds number	XFOIL High Reynolds number	XFOIL Design RE# High Turbulence
Power in, W	40.8	87.2	34.8	48.4
Power out, W	20.42	20.42	20.42	20.42
Efficiency (%)	50.0	23.4	58.6	42.2

4.2.5 Experimental Performance and Discussion

Experiments performed at Claytor Lake using the new propeller showed performance very similar to that predicted by Laitone data. Motor turns versus vehicle speed, speed versus electrical power into the

system and speed versus overall propulsive efficiency are shown in Figure **23**. Cruise at the design propeller turn rate of 2000 RPM resulted in a vehicle speed of 2.08 m/s, a power draw of 53 W, and an efficiency of 42.7%.

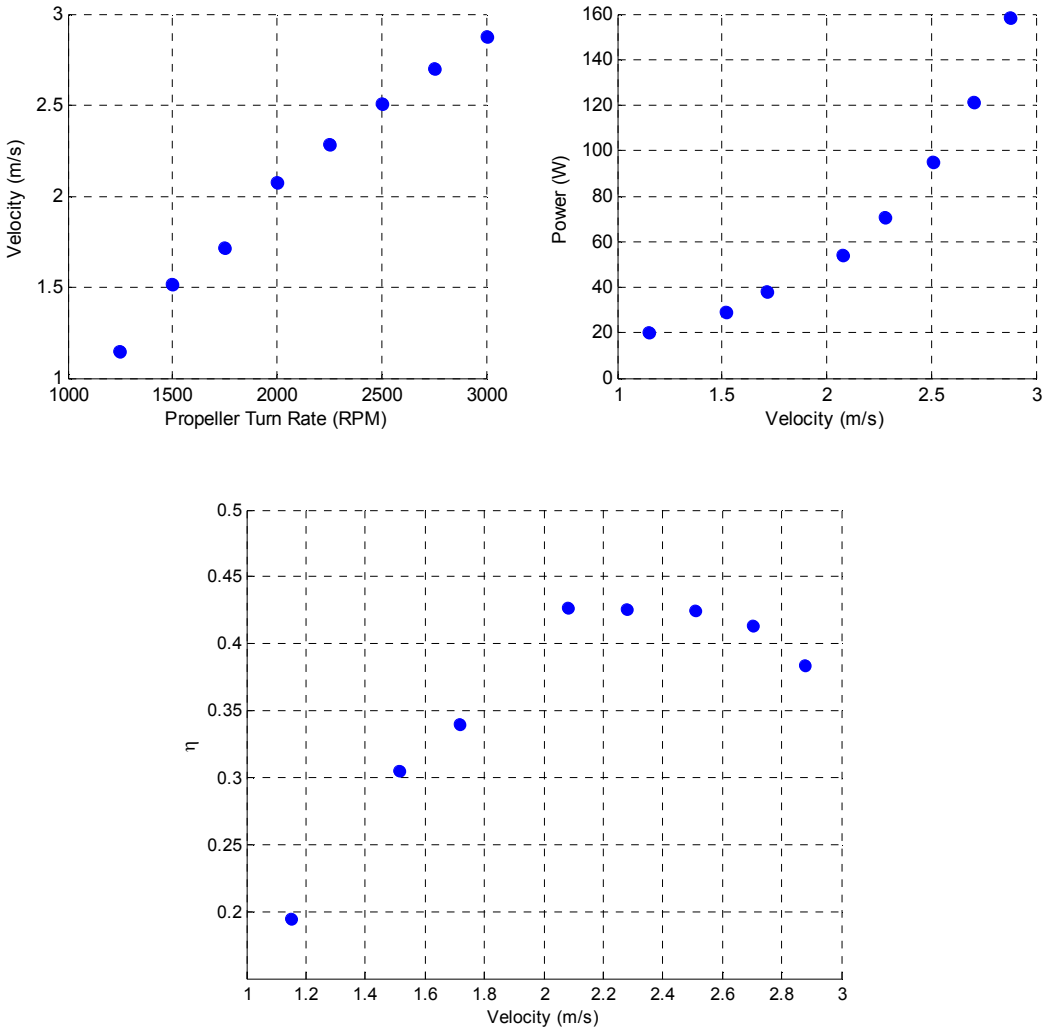

Figure 23. Claytor Lake experimental results using the new propeller design. The vehicle drag used for efficiency is calculated assuming it is purely quadratic in velocity and is based on the design point of 10.21 N at 2 m/s.

The high level of agreement between the OpenProp empirical based results and experimental results speaks well of the ability of lifting line theory near the design point. The difference in efficiency is likely due to actual vehicle drag being higher than that predicted using CFD, the propeller geometry not actually matching the 5% camber 1.4% thick plate from which the data was generated and the inaccuracy of the motor modeling; the motor controller efficiency is probably not 97% at a duty cycle of about 60%. These results suggest that it is best to use wind tunnel results for determining the lift and drag coefficients whenever possible.

The design Reynolds number low turbulence XFOIL based thrust prediction is once again the worst of the approaches taken. The high turbulence design Reynolds number based thrust prediction is also

pretty far off, but the efficiency is the most accurate of all techniques. The high Reynolds number XFOIL based torque prediction is comparably poor. The lift and drag curves given in Figure **18** show that the low Reynolds number XFOIL results predict drag relatively well, but not the lift. The opposite is true for the high Reynolds number XFOIL results. This suggests that the best prediction method is somewhere between the two. This was the initial motivating factor to explore the effect of inflow turbulence intensity. Since XFOIL uses the e^n transition prediction method the inflow turbulence level can be adjusted. To this point the amplification factor for low turbulence was 9, which corresponds to a clean wind tunnel and the high turbulence amplification factor was 0.95 roughly corresponding to 2% turbulence intensity. The propeller, in the wake of the 690, likely has high turbulence intensity corresponding to an amplification factor of less than 2. Experimental or computational data giving the turbulence level profile in the near wake of a Suboff body should be explored.

4.3 Complete Propulsion System Redesign

The final propulsion system design is a full system redesign for the 690. As per the design methodology described in Chapter 3, first a propeller was designed and then a motor and battery pack matched to it.

4.3.1 Propeller Design

The only requirement on the propeller is that it produces 10.21 N of thrust at 2 m/s forward velocity. Some additional design constraints from manufacturing considerations are that the minimum thickness is 0.6 mm.

Only a fairly small parametric study was performed. Table **13** describes the parameters and values over which they were varied.

Table 13. Parametric study parameters

Parameter	Value(s)
Diameter (m)	0.05, 0.075, 0.1, 0.125
Advance Ratio	0.3-0.9
Number of Blades	3, 5

The airfoil sections were designed using XFOIL with a turbulence level of 2.0% as given in section 3.1.2.5 with the airfoil section at each station chosen based on optimizing lift over drag given the required lift per unit span and incident velocity. XFOIL was chosen for airfoil design because CFD was deemed to slow and incapable of predicting transitional behavior and sufficient wind tunnel data for airfoils at low Reynolds number is not available. This airfoil design procedure gives the airfoil shape as well as the required angle of attack. The geometric pitch angle for each section is then the sum of the incident velocity direction as determined by the minimum induced loss optimizer in OpenProp and the required angle of attack.

As expected, the optimal propeller input power decreases with increasing diameter as shown in Figure **24**. Similarly, the power required also decreases with increasing advance ratio as shown in Figure **25**. This means that the most efficient propeller will be large and slow turning, a result consistent with momentum theory. A comparison of 3-bladed and 5-bladed propellers is given in Figure **26** showing that the minimum power is comparable between the two choices though it occurs at different advance ratios.

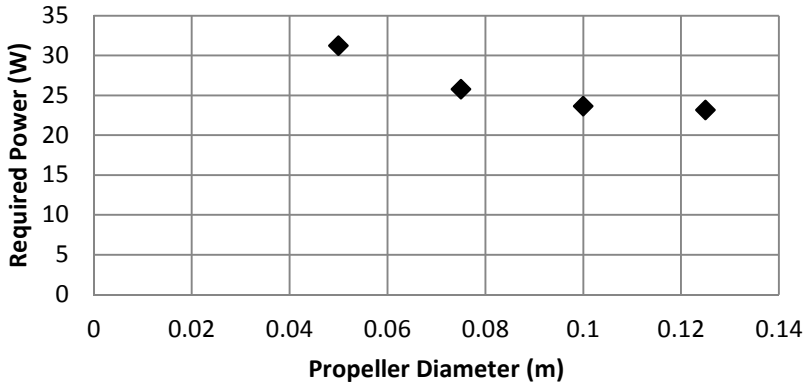

Figure 24. Parametric power required versus propeller diameter for the optimal propeller at each diameter. The required power drops with an increase in propeller diameter but diminishing returns are quickly reached. Other design considerations, such as keeping the propeller diameter smaller than that of the 690, restrict the maximum diameter.

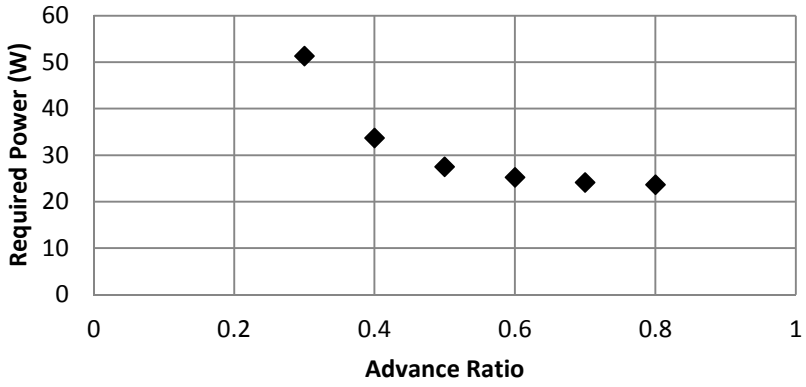

Figure 25. Parametric power required versus propeller advance ratio for an optimal 3-bladed propeller with diameter of 0.1 m. Increasing advance ratio reduces required power until a design is no longer feasible.

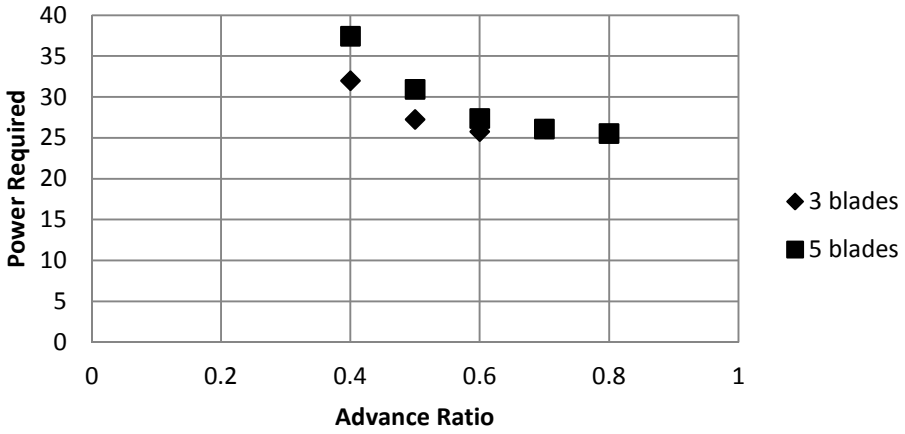

Figure 26. Comparison of the power required for 3 and 5-bladed propellers. For a given advance ratio the 3-bladed propeller always requires less power than the 5-bladed, but the 5-bladed propeller is capable of higher advance ratios. At higher advance ratios the 5-bladed propellers become as efficient as the 3-bladed propeller.

Through the parametric study two potential propeller designs were chosen, one a 3-bladed propeller and the other 5-bladed. The parameters describing the two propellers are given in the Table **14** and the propellers are shown in the Figure 27. The maximum camber, position of maximum camber, thickness to chord ratio, angle of attack and Reynolds number distribution are given in Figure **28** and Figure **29**. The advance ratio and diameter of each propeller were chosen to minimize the required power while also not being at the very edge of what was found possible by the minimum induced loss optimizer in OpenProp; given a propeller diameter and required thrust there is a minimum turn rate below which OpenProp will fail to converge to an optimal lift distribution

Table 14. Final propulsion system candidate propeller designs. The designs may change as a result of motor selection.

Parameter	**3-Bladed Propeller Value**	**5-Bladed Propeller Value**
K_T	0.120	0.197
K_Q	0.0160	0.0338
Propeller Efficiency	0.657	0.656
Torque Required (oz-in)	18.9	24.1
Advance Ratio	0.7	0.9
Propeller Turn Rate (RPM)	1715	1333
Diameter (m)	0.1	0.1

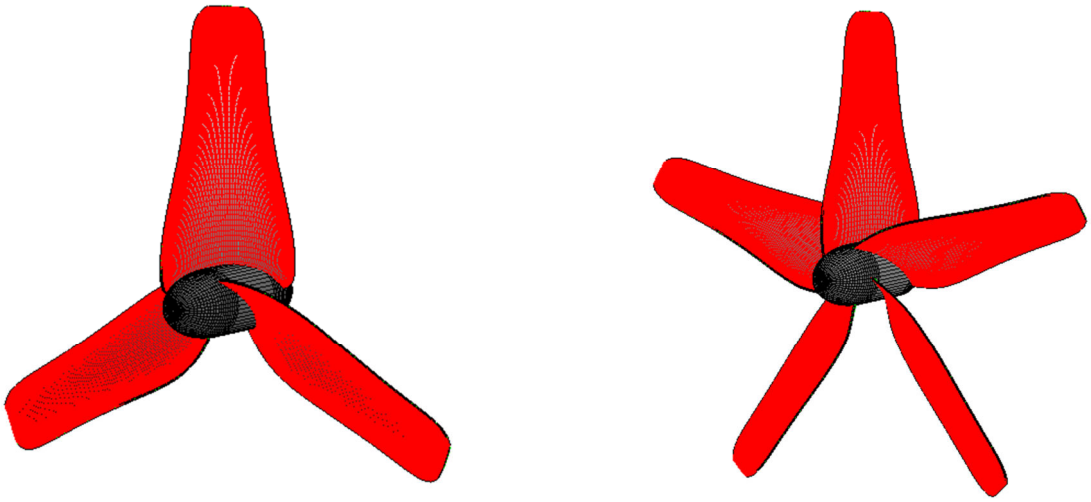

Figure 27. Propeller designs for the final propulsion system.

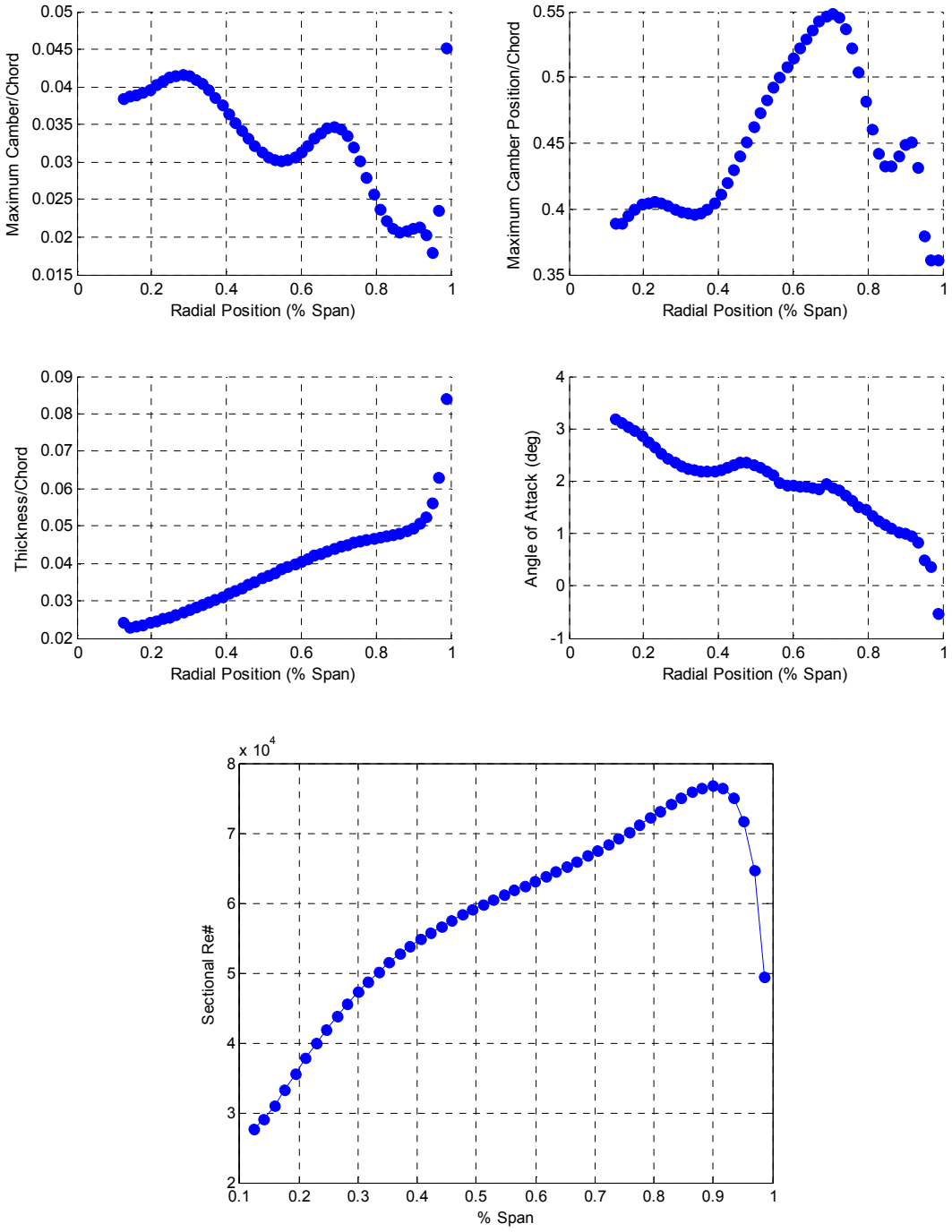

Figure 28. 3-bladed propeller geometry characteristics.

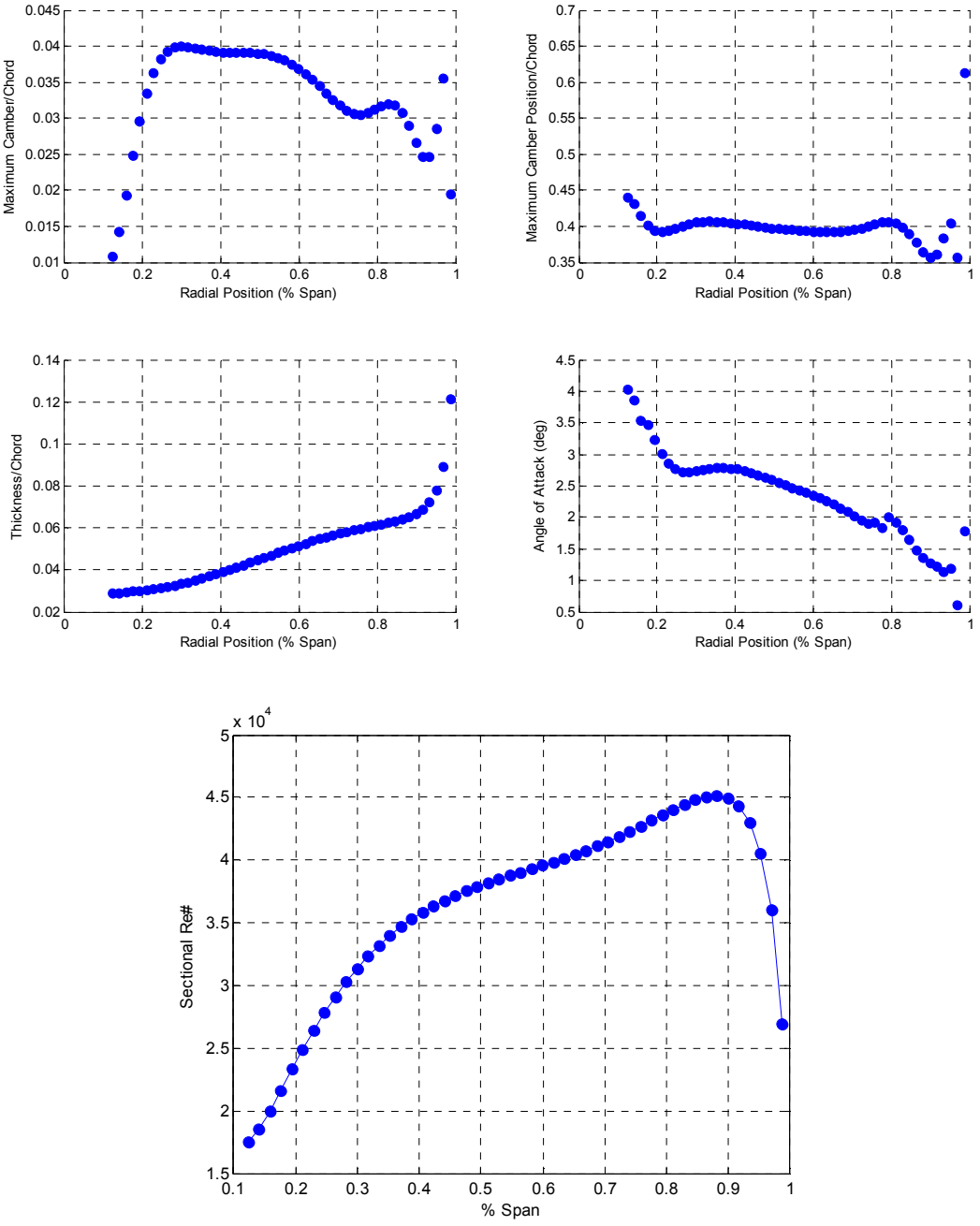

Figure 29. 5-bladed propeller geometry characteristics.

4.3.2 Motor & Battery Selection

The motor and battery are chosen such that they meet the requirements of the propeller and the rest of the 690 as efficiently as possible. Given the electronics the battery is required to power in addition to the propulsion system the supply voltage cannot be less than 6 V which will require 2 cells of the chosen batteries (Lithium-Ion LC-18650 38LG) in series. This gives a minimum voltage of 6 V, a minimum

nominal voltage of 7.5 V and a peak voltage of 8.6 V. The three-bladed propeller requires 18.9 oz-in of torque at 1715 RPM. Assuming the source voltage is much larger than the resistive voltage drop the approximate required motor constant is given by,

$$K_V = \frac{n}{V_s}. \tag{32}$$

Here, K_V is the RPS/V form of the motor constant, n is the motor and propeller required turn rate in rotations per second, and V_S is the battery supply voltage.

For the minimum source voltage this gives K_V = 285.8 RPM/V. The actual required K_V will be larger than this value, but it gives the approximate range of motor constants. In a large survey of available motors many were found with an appropriate K_V. The motors were then chosen for further analysis based on the amount of information available about the motor. Motor and voltage combinations were then analyzed giving a motor efficiency and required duty cycle for up to 6 series lithium-ion cells. A set of the better performing motor choices is given in Table **15**.

Table 15. Sample of motor survey and resulting motor calculations for the 3-bladed propeller. Motor efficiency and required duty cycle each number of battery cells in series at the minimum voltage.

Motor	Required Voltage	2 Cell Duty Cycle	3 Cell DC	4 Cell DC	5 Cell DC	6 Cell DC	Motor Efficiency
Neumotors - 1925 3Y	13.088	2.181	1.454	1.091	0.873	0.727	0.855
Neumotors - 1915-3Y	8.046	1.341	0.894	0.67	0.536	0.447	0.871
Neumotors - 1915-2Y	5.105	0.851	0.567	0.425	0.34	0.284	0.851
Scorpion HK 5020	3.973	0.662	0.441	0.331	0.265	0.221	0.83
Turnigy G60 Brushless	5.972	0.995	0.664	0.498	0.398	0.332	0.777
Neumotors 1917-1.5Y	4.528	0.755	0.503	0.377	0.302	0.252	0.817

Duty cycles of greater than 1 indicate the motor and battery combination will not be able to achieve the required turn rate at required torque. From the chart, three considerations are made to determine which motor to select. First, the motor efficiencies are compared. Second, cell count and motor combinations that result in high duty cycle are preferable over low duty cycle due to the loss of motor and controller efficiency at low duty cycle. And third, preference is given to lower total operating voltage in order to minimize other system losses due to regulating the battery voltage down to 3 V and 5 V where necessary. These considerations lead to choosing the Neumotors – 1915-3Y due to the high efficiency and high duty cycle with a 3 series cell battery pack.

Measured and calculated properties of the 1915-3Y at the effective voltage in the motor are given in Table **16**.

Table 16. Neumotors 1915-3Y motor physical characteristics and parameters at the required voltage for the 3-bladed propeller.

Parameter	Value
Length (in)	2.25
Weight (oz)	14
K_V (RPM/V)	225
K_Q (oz-in/A)	6.01
No-load Current (A)	0.34
Motor Resistance (Ohm)	0.1
Maximum Efficiency	0.87

Combining the propeller torque with the torque due to seals and oil in the tail, the total motor requirements and expected performance are given in Table **17**.

Table 17. Neumotors 1915-3Y predicted performance for the 3-bladed propeller.

Parameter	Value
Propeller, Seal and Oil Torque (oz-in)	23.4
Turn Rate (RPM)	1715
Required Effective/Motor Voltage (V)	8.05
Required Effective/Motor Current (A)	4.234
Resulting Motor Efficiency	0.87

A good motor for the 5-bladed propeller can be found similarly and is the Neumotors 1925-3Y with a 4 series cell battery pack operating at 0.864 duty cycle. The 1925-3Y physical characteristics and motor parameters are given in Table **18**. Performance of the 1925-3Y for the 5-bladed propeller is given in Table **19**.

Table 18. Neumotors 1925-3Y motor physical characteristics and parameters at the required voltage for the 5-bladed propeller.

Parameter	Value
Length (in)	3.3
Weight (oz)	22
K_V (RPM/V)	136
K_Q (oz-in/A)	9.94
No-load Current (A)	0.3
Motor Resistant (Ohm)	0.18
Maximum Efficiency	0.87

Table 19. Neumotors 1925-3Y predicted performance for the 5-bladed propeller.

Parameter	Value
Propeller, Seal and Oil Torque (oz-in)	28.6
Turn Rate (RPM)	1333
Required Effective/Motor Voltage (V)	10.38
Required Effective/Motor Current (A)	3.177
Resulting Motor Efficiency	0.86

The motor controller is currently modeled as having 97% efficiency regardless of duty cycle, but that likely is incorrect. Further study is required to determine the relationship between duty cycle and system efficiency but it is probably good practice to design for cruise at high duty cycle.

Another consideration when choosing a motor is that of its size and weight. As with all other systems on an AUV, the size and weight of the motor should be minimized to allow as much room and weight for payload and batteries. In the case of the 690 this is especially true for the motor due to the pressure-compensated motor housing. The pressure-compensated motor housing is very heavy relative to the rest of the vehicle and any reduction in size will result in a large relative weight reduction. The 690 currently requires a substantial amount of ballast weight in the vehicle nose to balance the motor housing, effectively wasting valuable vehicle buoyancy.

4.3.3 Predicted Performance

The overall system efficiency is simply calculated as power in over power out. Incorporating the 97% efficiency estimate of the motor controller the final efficiency estimates are given in Table **20**.

Table 20. Overall propulsion system efficiency estimates of the final propulsion system design.

Parameter	**3-Bladed Propeller Values**	**5-Bladed Propeller Values**
Power in (W)	35.1	34.0
Effective Power out (W)	20.42	20.42
Efficiency	0.581	0.601

Chapter 5 Summary and Future Work

5.1 Project Summary

A methodology for the design of small autonomous underwater vehicle propulsion systems has been developed and applied to the Virginia Tech 690 AUV. The methodology is novel in that it incorporates fast design level codes capable of predicting the viscous effects of the low Reynolds number flow that is experienced by small, slow turning propellers. The methodology consists of determining the minimum induced loss lift distribution for the propeller via lifting line theory, efficient airfoil sections for the propeller via a coupled viscous-inviscid flow solver and optimization, brushless DC motor identification via ideal motor theory and total system efficiency estimates. The coupled viscous-inviscid flow solver showed low Reynolds number flow effects to be of critical importance in the propeller design. The original Virginia Tech 690 AUV propulsion system was analyzed yielding an experimental efficiency of 26.5%. A new propeller was designed based on low Reynolds number airfoil section data yielding an experimental efficiency of 42.7%. Finally, an entirely new propulsion system was designed using the methodology developed herein yielding a predicted efficiency of 57-60%.

5.2 Future Work

There are a number of ways future work could enhance the present effort. A major remaining question is why the low Reynolds number XFOIL results for the first redesigned propeller seem to disagree with experimental results.

Future enhancements to this work should include manufacturing and testing the final propulsion system designs. Additionally, the improvements to the methodology may be made by the use RANS CFD and a better model of the brushless DC motor controller.

RANS CFD could be used to further analyze the propellers as designed. The individual airfoil sections as well as the entire propeller could be investigated. Unfortunately, the transitional nature of the flow at this scale would make using CFD very difficult. Transition and separation prediction are not currently mature capabilities of CFD.

Throughout the analysis and design of propulsion systems in this paper the motor controller has been assumed to be 97% efficient. This may be true at or near full throttle, but at partial throttle settings the total system losses will certainly be higher. Using pulse width modulation to reduce the effective voltage on the motor will result in additional switching losses as well as a less smooth current wave form. Modeling of these effects was investigated for this paper, but much of the literature found suggested the efficiency as a function of motor controller duty cycle would be highly dependent on the specific motor and motor controller used. This suggests experimental work is required.

Other areas of future design work potentially include moving from a lifting line based minimum induced loss optimization to a lifting surface optimization, a larger library of optimal airfoil sections specifically with non-constant thickness distributions, propeller structural design such that 3D printed propellers

could be used directly instead of requiring plating, and investigation into thrust augmentation devices such as ducts, pre-swirl vanes, endplates and propeller cone fins/boss cap fins.

Future work on analysis of propeller designs could include not only off-design performance but off-geometry performance. Since the manufacturing techniques are being pushed to the limit of their capabilities it is likely the designed geometries are not the exact geometries being fabricated. There is almost not control over leading and trailing edge geometry. Systematically understanding how 3D printed components may deform during fabrication and incorporating that into the design process to estimate bounds on divergence in performance due to geometry defects could be very interesting.

Works Cited

[1] W. D. Ramsey and W. M. Milewski, PSF10.3 User's Manual - Propeller Analysis Code with Vortex Wake Roll-up and Flow Adapted Gridding, Cambridge, MA: Massachusetts Insitute of Technology, Department of Ocean Engineering, 1997.

[2] J. Carlton, Marine Propellers and Propulsion, Burlington, MA: Elsevier Ltd., 2007.

[3] P. J. Kunz, "Aerodynamics and Design for Ultra-Low Reynolds Number Flight," Stanford University, Stanford, CA, 2003.

[4] R. W. Deters and M. S. Selig, "Static Testing of Micro Propellers," in *26th AIAA Applied Aerodynamics Conference*, Honolulu, HI, 2008.

[5] M. S. Selig, J. J. Guglielmo, A. P. Broeren and P. Giguere, Summary of Low-Speed Airfoil Data, vol. 1, Virginia Beach, VA: SoarTech Publications, 1995.

[6] M. P. Merchant, "Propeller Performance Measurement for Low Reynolds Number Unmanned Aerial Vehicle Applications," Wichita State University, Wichita, KS, 2004.

[7] J. M. Grasmeyer and M. T. Keennon, "Development of the Black Widow Micro Air Vehicle," AIAA, 2001.

[8] R. Turner, "Design and Optimization of a Propeller for a Micro Air Vehicle," 2010.

[9] J. A. Jacobson, "Using Single Propeller Performance Data to Predict Counter-Rotating Propeller Performance for a High Speed Autonomous Underwater Vehicle," Blacksburg, VA, 2007.

[10] J. A. Schultz, "Autonomous Underwater Vehicle (AUV) Propulsion System Analysis and Optimization," Blacksburg, VA, 2009.

[11] R. S. Duelley, "Autonomous Underwater Vehicle Propulsion Design," Blacksburg, VA, 2010.

[12] B. P. Epps and R. W. Kimball, "Unified Rotor Lifting Line Theory," *Journal of Ship Research,* vol. 57, no. 4, pp. 1-21, 2013.

[13] J. L. Hess and A. M. O. Smith, "Calculation of Non-Lifting Potential Flow About Arbitrary Three-dimensional Bodies," *Journal of Ship Research,* no. 8, pp. 22-44, 1964.

[14] J. Katz, A. Plotkin and , Low-Speed Aerodynamics, New York, NY: Cambridge University Press, 2006.

[15] W. B. Coney, "A Method for the Design of a Class of Optimum Marine Propulsors," Massachusetts Institute of Technology, Cambridge, MA, 1989.

[16] M. Drela and M. B. Giles, "Viscous-Inviscid Analysis of Transonic and Low Reynolds Number Airfoils," *AIAA Journal,* pp. 1347-1355, 1987.

[17] M. Drela, "XFOIL: An Analysis and Design System for Low Reynolds Number Airfoils," in *Conference on Low Reynolds Number Airfoil Aerodynamics*, University of Notre Dame, 1989.

[18] S. Brizzolara, D. Villa and S. Gaggero, "A systematic comparison between RANS and Panel Methods for Propeller Analysis," University of Genova, Department of Naval Architecture and Marine Engineering, Genova, ITA.

[19] E. V. Laitone, "Aerodynamic Lift at Reynolds Numbers Below 70,000," AIAA, Washington D.C., 1995.

[20] M. S. Selig, *Low Reynolds Number Airfoil Design Lecture Notes,* NATO Research and Technology Organization - Applied Vehicle Technology Panel, 2003.

[21] B. P. Epps, "OpenProp v2.4 Theory Document," MIT Department of Mechanical Engineering Technical Report, Cambridge, MA, 2010.

[22] J. J. Bertin and R. M. Cummings, Aerodynamics for Engineers, 5th ed., Upper Saddle River, NJ: Pearson Prentice Hall, 2008.

[23] R. Oliveira, "XFOIL - MATLAB interface - File Exchange - MATLAB Central," [Online]. Available: http://www.mathworks.com/matlabcentral/fileexchange/30478-xfoil-matlab-interface. [Accessed 20 July 2014].

[24] B. P. Epps and R. W. Kimball, "OpenProp v3: Open-source software for the design and analysis of marine propellers and horizontal-axis turbines," N/A, Hanover, NH, 2013.

[25] M. S. Selig, C. A. Lyon, P. Giguere, C. N. Ninham and J. J. Guglielmo, Summary of Low-Speed Airfoil Data, vol. 2, Virginia Beach, VA: SoarTech Publications, 1996.

[26] C. A. Lyon, A. P. Broeren, P. Giguere, A. Gopalarathnam and M. S. Selig, Summary of Low-Speed Airfoil Data, vol. 3, Virginia Beach, VA: SoarTech Publications, 1998.

[27] G. A. Williamson, B. D. McGranahan, B. A. Broughton, R. W. Deters, J. B. Brant and M. S. Selig, Summary of Low-Speed Airfoil Data, vol. 5, 2012.

[28] E. Larrabee, "Practical Design of Minimum Induced Loss Propellers," *SAE Technical Paper,* 1979.

Appendix A Momentum Theory Derivation

Make the following assumptions:

1. The flow is inviscid, irrotational, and incompressible (it is an ideal fluid).
2. The propeller can be thought of as an actuator disk with an infinite number of blades, each with infinite aspect ratio.
3. The propeller produces thrust without causing rotation of the slipstream.

The figure below shows the conceptual actuator disk at station (B), slipstream and stations far up (A) and downstream (C).

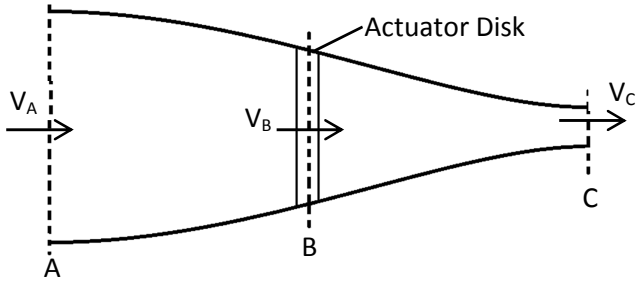

Figure 30. Momentum theory conceptual figure.

The thrust produced by the actual disk will be equal to the change in fluid momentum from A to C. That is,

$$T = \dot{m}(V_C - V_A). \tag{B.1}$$

Similarly, the power absorbed by the actuator disk is equal to the change in fluid kinetic energy from A to C,

$$P_D = \frac{1}{2}\,\dot{m}(V_C^2 - V_A^2), \tag{B.2}$$

While also being equal to the power being used to propel the ship,

$$P_D = TV_B. \tag{B.3}$$

Using equations (B.1) and (B.2) it can be easily seen that V_B is the average of V_A and V_C,

$$V_B = \frac{1}{2}(V_A + V_C). \tag{B.4}$$

The velocities at stations B and C can be written in terms of the velocity at station A with velocity increase terms, u_a and u_{a1},

$$\begin{aligned} V_B &= V_A + u_a, \\ V_C &= V_A + u_{a1}. \end{aligned} \tag{B.5}$$

Using equation (B.5), continuity and the assumption of incompressibility it can be shown the slipstream must contract,

$$Q_A = Q_B = Q_C \tag{B.6}$$

$$V_A A_A = V_B A_B = V_C A_C$$
$$V_A A_A = (V_A + u_a) A_B = (V_A + u_{a1}) A_C$$

Where $A_A = \frac{\pi D_A^2}{4}$, $A_B = \frac{\pi D^2}{4}$, and $A_C = \frac{\pi D_C^2}{4}$. Solving for the diameters at A and C,

$$D_A = \frac{V_A + u_a}{V_A} D^2,$$
$$D_C = \frac{V_A + u_{a1}}{V_A + u_{a1}} D^2. \tag{B.7}$$

Since $u_a > u_{a1}$ and are positive we can conclude that $D_A > D > D_C$.

Conservation of momentum states that the thrust is equal to the net outflow of momentum,

$$\rho V_A^2 A_A - \rho (V_A + u_{a1})^2 A_C + T = 0. \tag{B.8}$$

Using equations (B.6), (B.7) and (B.8) the thrust is the disk area times momentum at B times velocity increase from A to C,

$$T = \frac{\pi}{4} D^2 \rho (V_A + u_a) u_{a1} = \Delta p \, A, \tag{B.9}$$

That is, thrust is the product of the average slipstream area, average slipstream momentum and the change in flow velocity. Now, Bernoulli's equation can relate pressure and velocity upstream and downstream of the actuator disk (but not at the disk due to the discontinuity in pressure),

$$\frac{1}{2}\rho V_A^2 + p_A = \frac{1}{2}\rho (V_A + u_a)^2 + p_B,$$
$$\frac{1}{2}\rho (V_A + ua_1)^2 + p_C = \frac{1}{2}\rho (V_A + u_a)^2 + p_B + \Delta p, \tag{B.10}$$
$$p_A = p_C.$$

The difference between equations (B.10a,b) gives,

$$\Delta p = \frac{1}{2}\rho (2 V_A u_{a1} + u_{a1}^2). \tag{B.11}$$

Combining equations (B.4) and (B.5) the velocity increase from A to B is half of the increase from A to C,

$$\mathrm{u_a} = \frac{\mathrm{u_{a1}}}{2}. \tag{B.12}$$

Equations (B.9), (B.11) and (B.12) can be combined to provide additional forms of the thrust,

$$T = \frac{\pi}{4} D^2 \rho \left(V_A + \frac{u_{a1}}{2}\right) u_{a1},$$
$$T = \frac{\pi}{4} D^2 \rho (V_A + u_a) 2 u_a. \tag{B.13}$$

The thrust can be used in a dimensionless group to define a thrust coefficient,

$$C_T = \frac{T}{\frac{\pi}{4} D^2 \frac{1}{2} \rho V_A^2}, \tag{B.14}$$

which can be combined with the second of the additional thrust forms introduced above to provide an additional form of the thrust coefficient and the induced velocity,

$$C_T = \frac{(V_A + u_A)u_A}{V_A^2},$$
$$\frac{u_A}{V_A} = -\frac{1}{2} + \frac{1}{2}\sqrt{1 - C_T}. \tag{B.15}$$

The power representing the velocity induced aft of the disk is lost power and is given by,

$$P_{lost} = \rho(V_A + u_a)\left(\frac{\pi}{4}D^2\right)(2u_a)^2, \tag{B.16}$$

With first two terms representing the mass flow rate and the third term added velocity squared. The efficiency of the actuator disk can then be given as the power realized divided by the power used,

$$\eta = \frac{TV_A}{TV_A + P_{lost}}, \tag{B.17}$$

Finally, using equations (B.15), (B.16) and (B.17) the actuator disk efficiency is,

$$\eta = \frac{1}{1 + \frac{u_a}{V_A}},$$
$$\eta = \frac{2}{1 + \sqrt{1 + C_T}}. \tag{B.18}$$

The actuator disk efficiency represents the best possible efficiency for a propeller with the given thrust coefficient in the absence of viscous effects. This means it provides an upper bound on performance that will not be exceeded or even approached.

Appendix B Thin Airfoil Theory Parabolic Camber

For a full derivation of Thin Airfoil Theory see the derivation in [22].

The integral equation to be solved to determine the distribution of vortex strength is,

$$\frac{1}{2\pi}\int_0^{\pi}\frac{\gamma(\theta)\sin(\theta)\,d\theta}{\cos(\theta)-\cos(\theta_0)} = U_{\infty}\left(\alpha-\frac{dz}{dx}\right). \tag{C.1}$$

The desired vorticity distribution which satisfies (C.1) can be represented by a Fourier series where,

$$\begin{aligned} \mathrm{A}_0 &= \alpha-\frac{1}{\pi}\int_0^{\pi}\frac{dz}{dx}d\theta\,, \\ A_n &= 2/\pi\int_0^{\pi}\frac{dz}{dx}\cos(n\theta)d\theta. \end{aligned} \tag{C.2}$$

To find the aerodynamic coefficients of interest the relationships are,

$$\mathrm{C_l} = \pi(2\mathrm{A}_0+\mathrm{A}_1),\;\; C_{m0} = -\frac{\pi}{2}\left(A_0+A_1-\frac{A_2}{2}\right),\;\; X_{cp} = \frac{c}{4}\left(\frac{2A_0+2A_1-A_2}{2A_0+A_1}\right). \tag{C.3}$$

The specific example of a parabolic airfoil can be setup by writing the function $z(x)$,

$$\mathrm{z(x)} = ax^2+bx+c. \tag{C.4}$$

If we assume a chord of unit length, the parabolic function representing the camber line of the airfoil has the points (0,0) and (1,0). The remaining point to determine the coefficients a, b, and c can be chosen as the point of maximum camber (0.5, max camber)=($x_{c,max}$,$y_{c,max}$). Solving for a, b and c results in,

$$\mathrm{a} = -\frac{\mathrm{y_{c,max}}}{-x_{c,max}^2+x_{c,max}}, b = \frac{y_{c,max}}{-x_{c,max}^2+x_{c,max}}, c = 0. \tag{C.5}$$

Continuing with z(x), taking the derivative of z(x) with respect to x,

$$\frac{\mathrm{dz}}{\mathrm{dx}} = 2ax+b. \tag{C.6}$$

Using the transformation $x = \frac{1-\cos(\theta)}{2}$,

$$\mathrm{A}_0 = \alpha-\frac{1}{\pi}\int_0^{\pi}2ax+bx\,d\theta = \alpha \tag{C.7}$$

$$\mathrm{A}_1 = \frac{2}{\pi}\int_0^{\pi}\frac{dz}{dx}\cos(\theta)\,d\theta = -a \tag{C.8}$$

$$\mathrm{A}_2 = \frac{2}{\pi}\int_0^{\pi}\frac{dz}{dx}\cos(2\theta)\,d\theta = 0. \tag{C.9}$$

Using the elements of the Fourier series along with equations (C.3) the lift and moment coefficients along with the center of pressure location are given as,

$$\mathrm{C_l} = 2\pi\alpha-\pi\mathrm{a} = 2\pi\alpha-\pi\left(-\frac{\mathrm{y_{c,max}}}{-x_{c,max}^2+x_{c,max}}\right) \tag{C.10}$$

$$\mathrm{C_{m0}} = -\frac{\pi}{2}\alpha+\frac{\pi}{2}a = -\frac{\pi}{2}\alpha+\frac{\pi}{2}\left(-\frac{\mathrm{y_{c,max}}}{-x_{c,max}^2+x_{c,max}}\right) \tag{C.11}$$

$$\mathrm{x_{cp}} = \frac{1}{2}\left(\frac{\alpha-a}{2\alpha-a}\right) = \frac{1}{2}\left(\frac{\alpha+\frac{\mathrm{y_{c,max}}}{-x_{c,max}^2+x_{c,max}}}{2\alpha+\frac{\mathrm{y_{c,max}}}{-x_{c,max}^2+x_{c,max}}}\right) \tag{C.12}$$

Appendix C Lifting Line Theory

This derivation of lifting line theory follows [22], for full details see that text.

Assume that each section of a wing acts like an isolated two-dimensional section, and that spanwise flow is not great. Further assume that the section lift is related to the local circulation through the Kutta-Joukowski theorem, that is,

$$l(y) = \rho_\infty u_\infty \Gamma(y). \tag{D.1}$$

This means the spanwise lift distribution can be uniquely represented by a system of vortex filaments. Any change in the lift distribution will be represented by an associated change in vortex strength. Since vortex filaments cannot end in a fluid (per Helmholtz) the change is represented by vortex filaments turned $90°$ into the streamwise direction. This trailing system of vortex filaments is the wake and is assumed to extend to infinity for steady flows. This three sided vortex filament system is known as a 'horseshoe vortex'. For a transient analysis the trailing vortex filaments would end with the starting vortex.

As a result of Helmholtz' vortex theorems, the strength of the trailing semi-infinite vortex must be equal to the change in vortex strength from one section to the next. That is the trailing vortex strength is,

$$\Delta\Gamma = \frac{d\Gamma}{dy}\Delta y \tag{D.2}$$

The impact of a single semi-infinite vortex filament at y on the point y_1 is a velocity in the z direction,

$$\delta w_{y_1} = \frac{1}{2}\left[\frac{d\Gamma}{dy}dy\frac{1}{2\pi(y-y_1)}\right] \tag{D.3}$$

The cumulative impact of all of the semi-infinite vortex filaments which are the entire wing wake is,

$$w_{y_1} = \frac{1}{4\pi}\int_{-s}^{s}\frac{d\Gamma}{dy}\frac{1}{2\pi(y-y_1)}dy \tag{D.4}$$

For a typical lifting distribution with zero lift at the wing root and tip and monotonically increasing then decreasing this will result in w_{y_1} that is negative, that is a downward velocity. This induced velocity is known as the downwash. This results in a reduced effective angle of attack by the local downwash angle,

$$\epsilon(y_1) = \tan^{-1}\left(\frac{w_{y_1}}{u_\infty}\right) \tag{D.5}$$

Since the resultant velocity is inclined downward relative to the freestream direction a component of the lift is in the freestream direction as shown in Figure **31**. This is the lift induced drag.

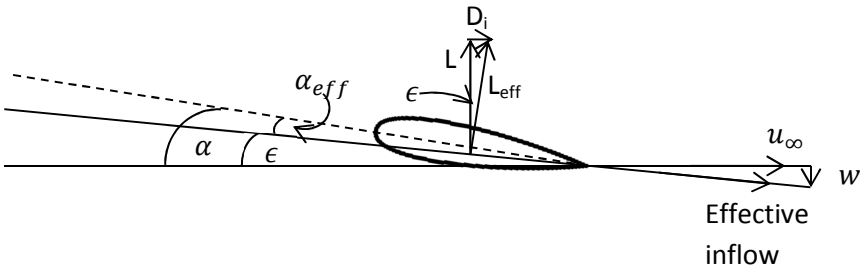

Figure 31. Lift induced drag diagram

Using (D.1), the downwash velocity and the freestream velocity the lift and induced drag on a wing are then,

$$L = \int_{-s}^{s} \rho_\infty u_\infty \Gamma(y)\, dy \tag{D.6}$$

$$D_i = \int_{-s}^{s} \rho_\infty \mathrm{w} \Gamma(y)\, dy \tag{D.7}$$

Appendix D Ideal Motor Theory Derivation

A simple model of a three phase motor is shown in **Figure 32**.

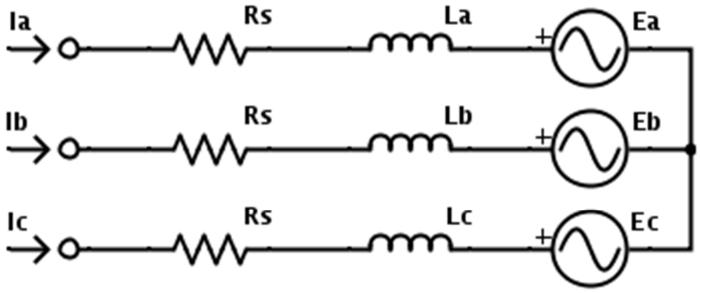

Figure 32. Simple three phase motor diagram

From **Figure 32** we can write the set of equations describing the motor circuit as,

$$\begin{bmatrix} V_{as} - v_n \\ V_{bs} - v_n \\ V_{cs} - v_n \end{bmatrix} = \begin{bmatrix} R_s & 0 & 0 \\ 0 & R_s & 0 \\ 0 & 0 & R_s \end{bmatrix} \begin{bmatrix} I_a \\ I_b \\ I_c \end{bmatrix} + \begin{bmatrix} L_{aa} & L_{ab} & L_{ac} \\ L_{ba} & L_{bb} & L_{bc} \\ L_{ca} & L_{cb} & L_{cc} \end{bmatrix} P\left(\begin{bmatrix} I_a \\ I_b \\ I_c \end{bmatrix} \right) + \begin{bmatrix} E_a \\ E_b \\ E_c \end{bmatrix}. \quad \text{(E.1)}$$

$P()$ is a time derivative and the inductance matrix reflects the interaction between coils. In the middle of a conduction cycle the current is assumed to be constant so (E.1) can be simplified to,

$$\begin{bmatrix} V_{as} - v_n \\ V_{bs} - v_n \\ V_{cs} - v_n \end{bmatrix} = \begin{bmatrix} R_s & 0 & 0 \\ 0 & R_s & 0 \\ 0 & 0 & R_s \end{bmatrix} \begin{bmatrix} I_a \\ I_b \\ I_c \end{bmatrix} + \begin{bmatrix} E_a \\ E_b \\ E_c \end{bmatrix}. \quad \text{(E.2)}$$

If only considering the conducting phases in (E.2) and take the neutral point voltage to be zero we have,

$$V_s = R_s I + E. \quad \text{(E.3)}$$

Faraday's Law of Induction says the electromotive force (EMF) is equal to $d\psi/dt$ where ψ is flux linkage,

$$E_i = \frac{d\psi}{dt} = \frac{d\psi}{d\theta}\frac{d\theta}{dt} = \frac{d\psi}{d\theta}\omega. \quad \text{(E.4)}$$

If we suppose that E_i is constant during a conduction cycle and then it follow from (E.4) that E_i for the two conducting phases can be written,

$$E_i = K_E \omega_m \quad \text{(E.5)}$$

where K_E is the motor's EMF constant. At constant speed, the constant torque waveform and the constant DC supply current waveform represent electromechanical energy conversion according to,

$$EI = T\omega_m \quad \text{(E.6)}$$

where E is the EMF across two phases in series. From (E.5) and (E.6) it follows,

$$T = K_E I. \quad \text{(E.7)}$$

When in the form of equation (E.7) K_E is often referred to as the torque constant, K_T. Now, using equations (E.3), (E.5) and (E.7) we can write,

$$\omega_m = \frac{1}{K_E}(V - R_s I). \quad \text{(E.8)}$$

Lastly, the efficiency of an ideal motor is given as power in over power out,

$$\eta = \frac{P_{in}}{P_{out}} = \frac{\omega_m T}{VI} = 1 - \frac{R_s}{V} I. \tag{E.9}$$

To summarize the ideal motor equations, at steady state during a conduction phase the motor angular rate is proportional to the EMF induced voltage, torque is proportional to the current and efficiency is a function of source voltage, current and motor resistance,

$$\omega_m = \frac{1}{K_E} E = \frac{1}{K_E} (V - R_s I) \tag{E.10}$$

$$T = K_E I \tag{E.11}$$

$$\eta = \frac{\omega_m T}{VI} = 1 - \frac{R_s}{V} I \tag{E.12}$$

The motor equations as they have been developed assume the motor has no inherent load and that if no external load is applied the current draw will be zero. This is unrealistic. To correct for this the notion of a no load current is introduced. The no load current is meant to represent the constant current required to operate the motor when no external load is provided. It can be introduced to the motor equations by modifying the torque-current relationship,

$$T = K_E (I - I_{nl}). \tag{E.13}$$

The no load current has the further impact of introducing a maximum efficiency of less than 100%. The new motor efficiency equation is,

$$\eta = \frac{\omega_m T}{VI} = \frac{(V - R_s I)(I - I_{nl})}{VI}. \tag{E.14}$$

The maximum efficiency can now be found by taking the derivative of (E.14) with respect to the current I and solving for the minimum.

$$\frac{d\eta}{dI} = \frac{RI^2 + VI_{nl}}{VI^2}, \tag{E.15}$$

$$I_{\eta,max} = \sqrt{\frac{VI_{nl}}{R_s}} \tag{E.16}$$

Using the current at maximum efficiency we can calculate the maximum efficiency and associated angular rate and torque,

$$\eta_{max} = \left(1 - \sqrt{\frac{I_{nl} R_s}{V}}\right)^2, \tag{E.17}$$

$$\omega_{m,\eta_{max}} = \frac{1}{K_E} \left(V - R_s I_{\eta_{max}}\right) \tag{E.18}$$

$$T_{\eta_{max}} = K_E \left(I_{\eta_{max}} - I_{nl}\right). \tag{E.19}$$

Appendix E Software Description and Code

A large amount of software was developed for this project, but the most important of it is the software that ties XFOIL and OpenProp together. A freely available interface between XFOIL and MATLAB is available from [23]. This interface as used with minor modifications. The code included here are the customized functions from OpenProp and the XFOIL-MATLAB interface as well as an example MATLAB propeller file and run script. The table below describes the various modifications to OpenProp and additional code written to interface OpenProp and XFOIL.

All of the functions borrow liberally from the original OpenProp MATLAB code.

Original Function	**Modified/New Function Name**	**Reason for Change/Purpose**
Example_input.m	Portner690prop.m	Specific prop for 690
	PortnerRunScript.m	Script to run propeller design codes
EppsOptimizer.m	EppsOptimizer_SMP.m	Allow new geometries and enforce geometry choices
GeometryFoil2D.m	GeometryFoil2D_SMP.m	Allow new geometries and enforce geometry choices
Geometry.m	Geometry_SMP.m	Allow new geometries and enforce geometry choices
	DesignSections_SMP.m	Interface with XFOIL and design sectional geometry
	BuildSTLGrid.m	Allow export of propeller geometry as STL files for 3D printing
	AnalyzePerformanceXFOIL.m	Off-design analysis of XFOIL designed propellers using XFOIL
	EvaluateLargeGeometrySet.m	Design space mapping script
	SingleGeo.m	Generate an XFOIL acceptable geometry from OpenProp geometry parameters
	SetupSingleXFOIL.m	Setup a single XFOIL calculation using the XFOIL-MATLAB interface software
XFOIL.m	XFOIL.m	The XFOIL-MATLAB interface software was modified to allow more XFOIL options to be used